The influence of stochastic interface defects on the effective thermal conductivity of fiber-reinforced composites

Yiwei Wang[a], Junjie Ye[a,b*], Lu Liu[a], Ziwei Li[a], Yang Shi[a,b], Juan Ma[a,b], Jianqiao Ye[c*]

[a] Research Center for Applied Mechanics, Xidian University, Xi'an 710071, China
[b] Shaanxi Key Laboratory of Space Extreme Detection, Xidian University, Xi'an 710071, China
[c] School of Engineering, Lancaster University, Lancaster LA1 4YW, UK

Abstract

In this paper, a novel microscopic modeling strategy is proposed to investigate the effective thermal conductivity of composites with consideration of stochastic interface defects. To this end, the subdomain boundary element method combined with asymptotic homogenization is proposed to effectively solve the thermal conduction problem. In order to accurately capture the heat flux on the boundary and the internal region in the representative volume element (RVE), a parameterized sub-cell is constructed to discretize the RVE. On this basis, the influence of stochastic interface defects on the thermal conductivity of composites is investigated by utilizing the Monte Carlo method. Specifically, the effect of the location, length, thickness, and area of the interface defects on the thermal conductivity is investigated. A proportional decrease in the transverse thermal conductivity coefficient is found for interface defect areas ranging from 1% to 10%.

Keywords: **Interface defect; Subdomain boundary element method; Composites; Effective thermal conductivity; Monte Carlo method**

1. Introduction

Fiber-reinforced composites (FRC) have been increasingly used in the automobiles, aerospace, bridges and railway applications. Considering the influence of ambient temperature variations, extensive attention has been given to heat-related issues of the FRC. However, heat transfer in composites is complex due to their inherent heterogeneity and diverse internal structures, which brings challenges to the study of these issues.

In the last few decades, various approaches have been proposed in the literature to evaluate the effective thermal conductivity of composites, including experimental analysis [1-2], theoretical models [3-4], and numerical models, such as Finite Element Method (FEM) [5-6], Extended Finite Element Method [7], Generalized Finite Difference Method [8], etc. Naturally, a composite material has complex and diverse internal structures that have to be simplified to model it either analytically or numerically. For example, by assuming that the size and shape of inclusions in the matrix material of a composite are all the same and the inclusions are distributed periodically within the matrix, a so-called representative volume element (RVE) can be conveniently selected to approximately represent the microstructure of material [9-11]. Thus, micro-scale models can be used to study the macroscopic physical properties of a composite material [12]. In this respect, Wang and Qin [13] investigated interface effects on the micro- and macro-thermal behaviors of square-pattern unidirectional FRC. Zhao et al. [14] developed a 2D finite volume method (FVM) to evaluate transverse thermal conductivity of continuous FRCs. To determine the effective thermal conductivity of short FRC, Vieira et al. [15] used hexahedral elements to discretize RVE at a microscopic scale. Although significant progress has been made, including the aforementioned, some concerns still remain. For instance, a very dense mesh is needed for a FEM or FVM model in the regions of concentrated heat flow or complex geometry, which has a significant negative impact

*Corresponding authors.
Email address: ronkey6000@sina.com (Junjie Ye)
j.ye2@lancaster.ac.uk (Jianqiao Ye)

on the computation efficiency. This becomes even more challenging when interface defects are considered, which inevitably requires more elements for the interphase layer.

Boundary element method (BEM) exhibits an attractive potential in solving heat transfer problems for composite materials. Compared to FEM and FVM, BEM only discretizes the boundary of a solution domain, which results in a significant reduction in the number of required discrete elements, so that a higher calculation efficiency can be achieved when the interfaces are considered [16]. Ochiai [17] demonstrated that three-dimensional heat conduction in non-homogeneous and functionally gradient materials can be studied approximately without the use of a domain integral by the triple-reciprocity BEM. Fahmy [18] developed a new boundary element formula for simulating nonlinear temperature distribution of electrons, ions, and phonons in carbon nanotube fiber-reinforced composites embedded with dense rigid line inclusions. It is, however, not convenient to use BEM in the domain of multiphase materials since it is normally difficult to obtain fundamental solutions for such heterogeneous materials. In recent years, the subdomain boundary element method (SBEM) was developed to divide a domain into many subdomains for a partitioned non-uniform media, where the media of each subdomain is uniform. For example, Oberg et al. [19] studied the thermal conductivity of two-dimensional materials with non-uniform composition using SBEM. Wang et al. [20] developed a fast SBEM for three-dimensional large-scale thermal analysis of FRC. Dong et al. [21] used SBEM and the Maxwell uniform scheme to calculate the effective thermal conductivity of two-dimensional and three-dimensional heterogeneous materials. Qu et al. [22] utilized the generalized self-consistent scheme in conjunction with the isogeometric SBEM to investigate effective thermal conductivity. Gong et al. [23] used integral equations to calculate the effective thermal conductivity of steady-state composites, considering only the temperature on the interface as the unknown. Sapucaia et al. [24] proposed an effective 2D pixel-based boundary element formula to calculate the effective thermal conductivity of heterogeneous materials by representing each pixel of a digital image as a subdomain with four boundary elements. The above research has significantly promoted the development and application of SBEM in investigating the effective thermal conductivity of composites. However, all the above studies assumed that interfaces were perfect, i.e., by ignoring the imperfections of the interfaces between the matrix and the fiber. Consequently, these simplified models resulted in less accurate predictions of the thermal conductivity.

During the manufacturing process of a FRC, defects inevitably form inside the composite. These defects can be classified, based on their location, into matrix, fiber, and interface defects. Among them, interface defects include delamination in composite laminates and defects between fiber and matrix [25], such as interfacial pores between matrix and fibers [26]. This is attributed to the different thermal expansion coefficients of the matrix and the fibers, as well as the challenges in process control. The interface studied in this paper specifically refers to the interface between fibers and matrix, a channel for transmitting thermal loads between different constituents. Early work almost exclusively introduced a third-phase material named the interphase layer between fibers and matrix to study the influence of interface defects. Hasselman et al. [27] investigated the effect of interface defects on heat transfer by incorporating an equivalent contact thermal resistance into the continuous boundary condition of heat flow. In the studies mentioned above, the interface defects are always simplified as a thin layer structure that surrounds the fibers, and the influence of interface defects can be introduced by changing effective thermal conductivity [28-29]. It has been recognized that the simplification of interface defects as a thin layer structure is not sufficiently accurate because the influence of the location of interface defects, which often leads to local concentration of heat flux, is ignored. This is also an important factor in the heat conduction analysis of composites. To address these concerns and improve the accuracy of heat transfer analysis in composites with interface defects, modeling interface defects with stochastic position needs to be further investigated. Apart from the location, the shape of interface defects also needs to be considered. In real situations, interface defects may be irregularly shaped and influenced by multiple factors. In theoretical or numerical analyses, interface defects may be idealized as defects of simpler geometric shape to facilitate calculation. The idealized shapes include but are not limited to hemispherical, semi-circular [30], and elliptical defects [31], etc. A sector ring can also be used as an idealized geometric model for interface defects, and it follows the well-known cavitation phenomenon in a variety of matrices [32].

This paper proposes a new computing framework that combines asymptotic homogenization theory with SBEM to calculate effective thermal conductivity of FRC with consideration of the influence of location, length, thickness, especially, the area of interface defects. The framework provides a new approach to improve the accuracy of the predicted thermal conductivity of composite materials with stochastic interfacial defects. The paper is organized as follows. Section 2 briefly introduces the asymptotic homogenization method and SBEM modeling, which is utilized to study thermal conductivity and steady-state heat transfer of composite materials. Section 3 focuses on studying the effect of fiber volume fraction (FVF) on the effective thermal conductivity and local heat flux field. The accuracy of the proposed method is verified by comparing it with experimental data. The temperature field and heat flux distribution are then studied. In Section 4, the node pair decoupling method is used to simulate interface defects, and the Monte Carlo method is implemented to describe the stochastic interface defects. Specifically, the influences of length ratio, thickness, and area of the defects are considered. Section 5 is the conclusion.

2. *Modeling process of continuous* FRC

2.1. The asymptotic homogenization with multi-scale method for heat conduction of FRC

For a typical periodic composite material, the multi-scale modeling process for FRC is shown in Fig.1, where a body of FRC occupying the region, Ω, described by the macro- coordinate system x_1-x_2-x_3 with boundary, Γ, as shown in Fig. 1(a). Γ consists of temperature boundary Γ_1 and heat flux boundary Γ_2, thus $\Gamma_1 \cup \Gamma_2 = \Gamma$ and $\Gamma_1 \cap \Gamma_2 = \varnothing$. At the microscopic scale, it is considered that the reinforcement phase is periodically distributed in the matrix. Fig. 1(b) shows the periodic fiber arrangement in the FRC. The RVE can be used as to a microscopic model for the analysis. Fig. 1(c) shows a selected RVE with a local coordinate system y_1-y_2-y_3. It is the periodical cell (Y) of the FRC.

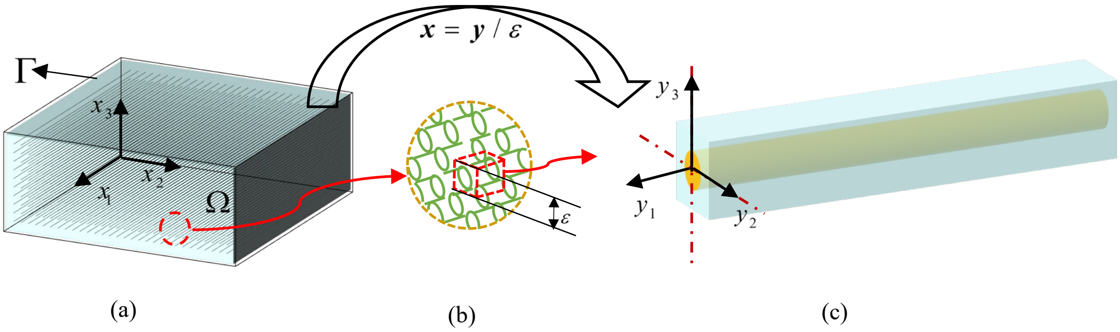

Fig. 1. Macro- and micro-structure of the composites: (a) FRC, (b) Periodical arrangements of the reinforced fibers, (c) RVE.

If the body shown in Fig.1(a) is a homogeneous media, as well known, the governing equation for steady-state heat conduction without internal heat sources can be expressed as:

$$\frac{\partial}{\partial x_i}\left[k_{ij}\frac{\partial T}{\partial x_j}\right]=0 \tag{1}$$

subjected to the following boundary conditions:

$$\begin{cases} T=T_0 & \text{on } \Gamma_1 \\ -k\dfrac{\partial T}{\partial \boldsymbol{n}}=\boldsymbol{q}_0 & \text{on } \Gamma_2 \end{cases} \tag{2}$$

where T_0 denotes temperature T on boundary Γ_1. $\boldsymbol{q}_0$ is a heat flux on boundary Γ_2. $\boldsymbol{n}=(n_1,n_2,n_3)$ is the unit outward normal vector of boundary Γ. $q_i=-k_{ij}\dfrac{\partial T}{\partial x_j}$ is the heat flux parameter, and k_{ij} denotes thermal conductivity.

As for the composite material shown in Fig. 1, the governing equation for the steady-state thermal conduction at a point of the composite without internal heat sources is:

$$\frac{\partial}{\partial x_i}\left[k_{ij}^{(\varepsilon)}\frac{\partial T^{(\varepsilon)}}{\partial x_j}\right]=0 \tag{3}$$

with the boundary conditions:

$$\begin{cases} T^{(\varepsilon)}=T_0 & \text{on } \Gamma_1 \\ -k_{ij}^{(\varepsilon)}\dfrac{\partial T^{(\varepsilon)}}{\partial \boldsymbol{n}}=\boldsymbol{q}_0 & \text{on } \Gamma_2 \end{cases} \tag{4}$$

Here ε is a perturbation parameter, which is associated with the characteristic dimension of inhomogeneity of the composite. For a periodic structure, ε is the dimension of the periodical cell (RVE), as seen in Fig. 1. Since the characteristic dimension of the periodic cell to the macroscopic body Ω is very small. ε is a very small positive number, i.e., $0<\varepsilon<<1$. Mathematically, this fact is formalized in the form $\varepsilon\to 0$ [33]. The heterogeneous macrostructure of the composite can be regarded as a homogeneous macrostructure.

The relationship between the macroscopic scale coordinate $\boldsymbol{x}$ and the micro scale coordinate $\boldsymbol{y}$ for the periodical structure can be expressed as:

$$\boldsymbol{y} = \boldsymbol{x} / \varepsilon \tag{5}$$

Due to the assumption of periodicity, the thermal conductivity coefficient, $k_{ij}^{(\varepsilon)}$ can be described by periodic functions in spatial variable of the following form:

$$k_{ij}^{(\varepsilon)} = k_{ij}\left(\boldsymbol{x} / \varepsilon\right) = k_{ij}\left(\boldsymbol{y}\right) \tag{6}$$

A direct numerical solution of Eq. (3) is challenging due to the rapid oscillation of the coefficients $k_{ij}^{(\varepsilon)}$. The asymptotic homogenization theory provides an alternative approach to solve the problem. Mathematically, by letting $\varepsilon \to 0$, the weak limit of differential Eq. (3) results in:

$$\frac{\partial}{\partial x_i}\left[k_{ij}^H \frac{\partial T}{\partial x_j}\right] = 0 \tag{7}$$

with the boundary condition:

$$\begin{cases} T = T_0 & \text{on } \Gamma_1 \\ -k_{ij}^H \dfrac{\partial T}{\partial \boldsymbol{n}} = \boldsymbol{q}_0 & \text{on } \Gamma_2 \end{cases} \tag{8}$$

where k_{ij}^H is the homogenized constant tensors, i.e., effective thermal conductivity, T is the homogenized temperature. As a result, Eq. (3) is reduced to the steady-state heat conduction problem of a homogenized material [33].

The temperature $T^{(\varepsilon)}\left(\boldsymbol{x}\right)$ can be expressed as an asymptotic expansion of the small parameter ε, that is:

$$T^{(\varepsilon)}\left(\boldsymbol{x}\right) = T^{[0]}\left(\boldsymbol{x},\boldsymbol{y}\right) + \varepsilon T^{[1]}\left(\boldsymbol{x},\boldsymbol{y}\right) + \varepsilon^2 T^{[2]}\left(\boldsymbol{x},\boldsymbol{y}\right) + \cdots \tag{9}$$

where $\boldsymbol{y} = \boldsymbol{x} / \varepsilon$ is the "fast" variable and $\boldsymbol{x}$ is the "slow" variable of a two-scale expansion. n is the asymptotic order.

By $\boldsymbol{y} = \boldsymbol{x} / \varepsilon$, there exists the following chain rule:

$$\frac{\partial}{\partial x_i} \to \frac{\partial}{\partial x_i} + \frac{1}{\varepsilon}\frac{\partial}{\partial y_i} \tag{10}$$

After inserting Eq. (10) and Eq. (9) into Eq. (3), the following equation is obtained by organizing the terms in terms of the same order of ε:

$$\begin{aligned} &\varepsilon^{-2}\left[L_1 T^{[0]}\left(\boldsymbol{x},\boldsymbol{y}\right)\right] + \varepsilon^{-1}\left[L_1 T^{[1]}\left(\boldsymbol{x},\boldsymbol{y}\right) + L_2 T^{[0]}\left(\boldsymbol{x},\boldsymbol{y}\right)\right] \\ &+\varepsilon^{0}\left[L_1 T^{[2]}\left(\boldsymbol{x},\boldsymbol{y}\right) + L_2 T^{[1]}\left(\boldsymbol{x},\boldsymbol{y}\right) + L_3 T^{[0]}\left(\boldsymbol{x},\boldsymbol{y}\right)\right] + \varepsilon^{1}\left[\cdots\right] + \cdots = 0 \end{aligned} \tag{11.1}$$

where,

$$L_1 = -\frac{\partial}{\partial y_i} k_{ij}\left(\boldsymbol{x},\boldsymbol{y}\right)\frac{\partial}{\partial y_j},\ L_2 = -\frac{\partial}{\partial y_i} k_{ij}\left(\boldsymbol{x},\boldsymbol{y}\right)\frac{\partial}{\partial x_j} - \frac{\partial}{\partial x_i} k_{ij}\left(\boldsymbol{x},\boldsymbol{y}\right)\frac{\partial}{\partial y_j},\ L_3 = -\frac{\partial}{\partial x_i} k_{ij}\left(\boldsymbol{x},\boldsymbol{y}\right)\frac{\partial}{\partial x_j}. \tag{11.2}$$

To be identical to zero, each factor of the power of ε in Eq. (11) must be equal to zero. For example, for ε^{-2}, $L_1 T^{[0]}(\boldsymbol{x},\boldsymbol{y})=0$. Therefore, $T^{[0]}$ is only a function of $\boldsymbol{x}$, independent of the microscopic coordinate $\boldsymbol{y}$. Thus Eq. (9) can be rewritten as [33-35]:

$$T^{(\varepsilon)}(\boldsymbol{x})=T^{[0]}(\boldsymbol{x})+\sum_{n=1}^{\infty}\varepsilon^{n}T^{[n]}(\boldsymbol{x},\boldsymbol{y}) \tag{12}$$

Functions $T^{[n]}(\boldsymbol{x},\boldsymbol{y})$ are assumed to be periodical in terms of $\boldsymbol{y}$. Function $T^{[0]}(\boldsymbol{x})$ is a function of $\boldsymbol{x}$, and is the homogenized temperature solution of Eq. (7).

The first order solution of $T^{[1]}(\boldsymbol{x},\boldsymbol{y})$ associated with the term of ε^{-1} in Eq. (11) can be written as,

$$T^{[1]}(\boldsymbol{x},\boldsymbol{y})=\chi^{j}(\boldsymbol{y})\frac{\partial T^{[0]}}{\partial x_j} \tag{13}$$

where $\chi^{j}(\boldsymbol{y})$ is the characteristic function which is only related to the microscopic scale coordinate, independent of the macroscopic scale coordinate system, and the periodicity in $\boldsymbol{y}$ with periodical cell (RVE)Y, which is given by:

$$\begin{cases} -\dfrac{\partial}{\partial y_i}\left(k_{iq}\dfrac{\partial \chi^{j}(\boldsymbol{y})}{\partial y_q}\right)=\dfrac{\partial}{\partial y_i}k_{ij}, & y\in Y \\ \chi^{j}(\boldsymbol{y})=0, & y\in \partial Y \end{cases} \tag{14}$$

The homogenized thermal conductivity coefficient can be defined by the characteristic function $\chi^{j}(\boldsymbol{y})$:

$$k_{ij}^{H}=\frac{1}{|Y|}\int_{Y}\left(k_{ij}+k_{iq}\frac{\partial \chi^{j}(\boldsymbol{y})}{\partial y_q}\right)dY \tag{15}$$

where $|Y|$ is the volume of the RVE.

Eq. (14) can be converted into the following form,

$$-\frac{\partial}{\partial y_i}\left(k_{iq}\left(\frac{\partial \chi^{j}(\boldsymbol{y})}{\partial y_q}+\frac{\partial \gamma^{j}(\boldsymbol{y})}{\partial y_q}\right)\right)=0 \tag{16}$$

where $\dfrac{\partial \gamma^{j}(\boldsymbol{y})}{\partial y_q}=\delta_{jq}$ is the temperature gradient along y_q, and $\delta_{jq}\,(j,q=1,\ 2,\ 3)$ is the Kronecker tensor. Moreover, the temperature gradient vector $\nabla\gamma_q^{j}=\dfrac{\partial \gamma^{j}}{\partial y_q}$ can be further expressed explicitly as:

$$\nabla\gamma^1 = \begin{Bmatrix} 1 \\ 0 \\ 0 \end{Bmatrix} \nabla\gamma^2 = \begin{Bmatrix} 0 \\ 1 \\ 0 \end{Bmatrix} \nabla\gamma^3 = \begin{Bmatrix} 0 \\ 0 \\ 1 \end{Bmatrix} \tag{17}$$

Considering Eq. (17), the right-hand side of Eq. (14) can be further expressed as follows:

$$\frac{\partial}{\partial y_i} k_{ij} = \frac{\partial}{\partial y_i} k_{iq} \nabla \gamma_q^j \tag{18}$$

Eq. (16) can be further simplified as,

$$\frac{\partial}{\partial y_j}\left(k_{iq}\nabla\left(W_q^j\right)\right) = 0 \tag{19}$$

where $W^j = \chi^j + \gamma^j$.

The boundary conditions are specified by Eq. (17). The temperature on the boundary of the RVE is subjected to the unit average temperature gradients with only one nonzero component in the respective coordinate directions. The effective thermal conductivity Eq. (15) can be then expressed as:

$$\begin{aligned} k_{ij}^H &= \frac{1}{|Y|}\int_Y \left(k_{ij} + k_{iq}\nabla\left(\chi_q^j\right)\right) dY \\ &= \frac{1}{|Y|}\int_Y \left(k_{ij} + k_{iq}\nabla\left(W_q^j - \gamma_q^j\right)\right) dY \\ &= \frac{1}{|Y|}\int_Y \left(k_{iq}\nabla\left(W_q^j\right)\right) dY \\ &= -\frac{1}{|Y|}\int_Y q_i \, dY \end{aligned} \tag{20}$$

where q_i is the flux components corresponding to W^j. This paper employs the subdomain boundary element method to solve the heat flux within an RVE numerically. Initially, the boundary integral equation with periodical boundary conditions is discretized. In a steady-state condition, at the interfaces between the matrix and fibers, the temperatures are considered the same in both materials. Thus, the heat fluxes and temperatures of all the elements on the boundary and interface can be calculated. Next, the temperature and heat flux at any internal point of the RVE can be calculated by following the standard boundary element solution procedure. Finally, the homogenized tensor k_{ij}^H can be calculated by Eq. (20), which is detailed in Section 2.2 and 2.3.

2.2. SBEM for composites

Based on the analysis presented in the previous section, the asymptotic homogenization approach converts the solution of a steady-state heat conduction problem (Eq. (3)) into a local unit cell problem (Eq. (14)) and a macroscopic homogenization problem (Eq. (20)), effectively alleviating the complexity associated with directly solving multiscale heat conduction problems using numerical methods. Compared with other domain methods, the unique feature of the boundary element method is that it only requires mesh partitioning at the boundaries or internal interfaces of the solution region. Moreover, while maintaining a high accuracy, the number of degrees of freedom in a boundary element discretization is significantly fewer than that in a finite element discretization. Consequently, employing the BEM to solve unit cell problems not only simplifies the task of meshing these cells but also drastically reduces the cost of the computation, thereby significantly enhancing computational efficiency. The following sections present the discretization process and the algorithmic workflow for the BEM.

To solve the first-order cell problem using the BEM, it is required to formulate the boundary integral equation corresponding to Eq. (14), which χ^j satisfies. For the boundary integral equation that satisfies Eq. (14), the fundamental solution satisfies Eq. (21) is [35]:

$$\int_{\Omega} k(Q)T(Q)\frac{\partial}{\partial y_i}\left(\frac{\partial u^*(Q,P)}{\partial y_i}\right)d\Omega = -k(P)T(P) \tag{21}$$

where Q and P are the field point and source point, respectively; $T(P)$ is the temperature at source point P; $q(Q)$ is the heat flux at the field point Q; $u^*(Q,P)$ is the fundamental solution of the two- dimension (2D) or three-dimension (3D) problem, as follows:

$$u^*(Q,P) = \begin{cases} \dfrac{1}{2\pi}\text{In}\left(\dfrac{1}{r}\right) & \text{for 2D problems} \\ \dfrac{1}{4\pi r} & \text{for 3D problems} \end{cases} \tag{22}$$

In Eq. (22), r is the distance between P and Q.

Using the fundamental solution u^* as the weight function and integrating Eq. (14) result in:

$$\int_Y u^*(Q,P)\frac{\partial}{\partial y_i}\left(k_{iq}\frac{\partial \chi^j}{\partial y_q}\right)dY + \int_Y u^*(Q,P)\frac{\partial k_{ij}}{\partial y_i}dY = 0 \tag{23}$$

Integrating by parts the first integral in Eq. (23) and considering the Gauss divergence theorem and the fundamental solution, the integration of the left-hand-side of Eq. (23) becomes:

$$\begin{aligned} \int_Y u^*(Q,P)\frac{\partial}{\partial y_i}\left(k(Q)\frac{\partial \chi^j(Q)}{\partial y_q}\right)dY &= -C(P)k(P)\chi^j(P) - \int_{\partial Y} u^*(Q,P)q(Q)dS \\ &- \int_{\partial Y}\frac{\partial u^*(Q,P)}{\partial \boldsymbol{n}}k(Q)\chi^j(Q)dS + \int_Y \frac{\partial u^*(Q,P)}{\partial y_i}\frac{\partial k}{\partial y_i}\chi^j(Q)dY \end{aligned} \tag{24}$$

where $q(Q)=-k(Q)\dfrac{\partial \chi^j(Q)}{\partial \boldsymbol{n}}$, $q^*(Q,P)=\dfrac{\partial u^*(Q,P)}{\partial \boldsymbol{n}}=\begin{cases}-\dfrac{1}{2\pi r}\dfrac{\partial r}{\partial \boldsymbol{n}} & \text{for 2D problems}\\ -\dfrac{1}{4\pi r^2}\dfrac{\partial r}{\partial \boldsymbol{n}} & \text{for 3D problems}\end{cases}$.

Then, the integral equation associated to the characteristic function can be obtained:

$$\begin{aligned}-C(P)k(P)W^j(P)=&\int_{\partial Y}u^*(Q,P)q(Q)dS+\int_{\partial Y}q^*(Q,P)k(Q)W^j(Q)dS\\&-\int_Y \frac{\partial u^*(Q,P)}{\partial y_i}\frac{\partial k(Q)}{\partial y_i}W^j(Q)dY\end{aligned} \tag{25}$$

where $C(P)=1-\dfrac{\theta}{2\pi}$ is the geometric coefficient at the source point P; θ is the external angle of the boundary at point P. The boundary is assumed to be smooth, thus, C is 0.5.

The first two terms in Eq. (25) are boundary integrals, while the other integrals in the equation are domain integrals that are the results of the varying thermal conductivity of the heterogeneous materials. In this study, the domain integrals can be avoided by using the subdomain boundary element method (SBEM) that establishes boundary integral equations for fibers and matrix separately.

By SBEM. The solution domain can be further divided into several sub-regions according to the computational needs, over which the respective boundary integral equations are established. Naturally, new equations on the interfaces between the adjacent regions are formed.

A two-dimensional model of the RVE is shown in Fig. 2. The boundary integral equations for the matrix and fiber can be established as,

$$C(P)u^{\mathrm{A}}(P)+\int_{\Gamma'\cup\Gamma''}q^*(Q,P)u^{\mathrm{A}}(Q)d\Gamma(Q)=-\int_{\Gamma'\cup\Gamma''}u^*(Q,P)q^{\mathrm{A}}(Q)d\Gamma(Q) \tag{26}$$

$$C(P)u^{\mathrm{B}}(P)+\int_{\Gamma''}q^*(Q,P)u^{\mathrm{B}}(Q)d\Gamma(Q)=-\int_{\Gamma''}u^*(Q,P)q^{\mathrm{B}}(Q)d\Gamma(Q) \tag{27}$$

where, $u=k\chi^j$, and the matrix contains the outer boundary Γ' and the inner boundary Γ'', the latter represents the common boundary between fibers and matrix. The superscripts A and B denote matrix and fiber, respectively. The outer boundary Γ' consists of temperature boundary Γ'_1 and heat boundary Γ'_2.

Eqs. (26) -(27) are further expressed in a matrix form, that is,

$$\begin{bmatrix}\mathbf{H}_1^{\mathrm{A}} & \mathbf{H}_2^{\mathrm{A}}\end{bmatrix}\begin{Bmatrix}\mathbf{u}_1^{\mathrm{A}}\\ \mathbf{u}_2^{\mathrm{A}}\end{Bmatrix}=\begin{bmatrix}\mathbf{G}_1^{\mathrm{A}} & \mathbf{G}_2^{\mathrm{A}}\end{bmatrix}\begin{Bmatrix}\mathbf{q}_1^{\mathrm{A}}\\ \mathbf{q}_2^{\mathrm{A}}\end{Bmatrix} \tag{28}$$

or

$$\mathbf{H}^{\mathrm{B}}\mathbf{u}^{\mathrm{B}}=\mathbf{G}^{\mathrm{B}}\mathbf{q}^{\mathrm{B}} \tag{29}$$

where matrix $\mathbf{H}$ contains the integrals of heat flux fundamental solution q^* on the boundary. The matrix $\mathbf{G}$ contains the integrals of temperature fundamental solution u^* on the boundary. $\mathbf{u}_1^{\mathrm{A}}$

and $\mathbf{q}_1^{\mathrm{A}}$ are the nodal temperatures and heat fluxes on the external boundary Γ', respectively. $\mathbf{u}_2^{\mathrm{A}}$ and $\mathbf{q}_2^{\mathrm{A}}$ are the nodal temperatures and heat fluxes at the interface Γ''. From the continuity of the temperatures and the equilibrium conditions of the heat flux, one has the following relations:

$$\mathbf{u}_2^{\mathrm{A}} = \mathbf{u}^{\mathrm{B}} \tag{30}$$

$$\mathbf{q}_2^{\mathrm{A}} = -\mathbf{q}^{\mathrm{B}} \tag{31}$$

$$\mathbf{q}_2^{\mathrm{A}} = -\left(\mathbf{G}^{\mathrm{B}}\right)^{-1} \mathbf{H}^{\mathrm{B}} \mathbf{u}_2^{\mathrm{A}} \tag{32}$$

Let,

$$\mathbf{QU} = -\left(\mathbf{G}^{\mathrm{B}}\right)^{-1} \mathbf{H}^{\mathrm{B}} \tag{33}$$

Thus, Eq. (32) becomes,

$$\mathbf{q}_2^{\mathrm{A}} = \left[\mathbf{QU}\right] \mathbf{u}_2^{\mathrm{A}} \tag{34}$$

Substituting Eq. (34) into Eq. (28) yields:

$$\left[\mathbf{H}_1^{\mathrm{A}} \quad \mathbf{H}_2^{\mathrm{A}} - \mathbf{G}_2^{\mathrm{A}}\left[\mathbf{QU}\right]\right] \begin{Bmatrix} \mathbf{u}_1^{\mathrm{A}} \\ \mathbf{u}_2^{\mathrm{A}} \end{Bmatrix} = \mathbf{G}_1^{\mathrm{A}} \mathbf{q}_1^{\mathrm{A}} \tag{35}$$

After applying the periodic temperature boundary conditions to all the nodes of the outer boundary Γ' of the RVE, Eq. (35) can be rearranged and expressed in the form of the following linear algebraic equations:

$$[A]\{X\} = \{F\} \tag{36}$$

Where $\{X\}$ is a vector containing the unknown nodal temperature and heat flux on the boundary.

From Eq. (22), it can be obtained that:

$$u_{,i}^{*}(Q,P) = \frac{\partial u^{*}(Q,P)}{\partial x_i} = \begin{cases} -\dfrac{r_{,i}}{2\pi r} & \text{for 2D problems} \\ -\dfrac{r_{,i}}{4\pi r^2} & \text{for 3D problems} \end{cases} \tag{37}$$

where r and $r_{,i}$ are, respectively:

$$r = \sqrt{\sum_{i=1}^{\beta} \left(x_i^Q - x_i^P\right)^2} \tag{38}$$

$$r_{,i} = \frac{\partial r}{\partial x_i^Q} = \frac{x_i^Q - x_i^P}{r} \tag{39}$$

In which β is the dimension of the problem, and $\begin{cases} \dfrac{\partial r}{\partial x_i^Q} = \dfrac{x_i^Q - x_i^P}{r} = r_{,i} \\ \dfrac{\partial r}{\partial x_i^P} = -\dfrac{x_i^Q - x_i^P}{r} = -r_{,i} \end{cases}$.

Therefore,

$$\frac{\partial u^*}{\partial x_i^P} = \frac{\partial u^*}{\partial r}\frac{\partial r}{\partial x_i^P} = \left(-\frac{1}{2\pi r}\right)\left(-r_{,i}\right) = \frac{r_{,i}}{2\pi r} \tag{40a}$$

$$\frac{\partial u^*}{\partial x_i^Q} = \frac{\partial u^*}{\partial r}\frac{\partial r}{\partial x_i^Q} = \left(-\frac{1}{2\pi r}\right)\left(r_{,i}\right) = -\frac{r_{,i}}{2\pi r} \tag{40b}$$

From Eq. (40a) and Eq. (40b), it is noted that $\frac{\partial u^*}{\partial x_i^P} = -\frac{\partial u^*}{\partial x_i^Q}$. Furthermore, the heat flux at an internal point can be calculated by:

$$q_i(P) = -\int_\Gamma u_{,i}^*(Q,P)q(Q)d\Gamma(Q) - \int_\Gamma q_{,i}^*(Q,P)q(Q)d\Gamma(Q) \tag{41}$$

where the fundamental solution $q_{,i}^*$ can be derived from Eq. (42):

$$q_{,i}^*(Q,P) = \frac{\partial}{\partial x_i}\left(\frac{\partial u^*}{\partial \boldsymbol{n}}\right)\begin{cases} -\dfrac{1}{2\pi r^2}\left[n_i - 2r_{,i}r_{,j}n_j\right] & \text{for 2D problems} \\ -\dfrac{1}{4\pi r^3}\left[n_i - 3r_{,i}r_{,j}n_j\right] & \text{for 3D problems} \end{cases} \tag{42}$$

2.3. Discretization of the RVE

A two-dimensional model of the RVE (Fig. 2(a)) is discretized by the boundary elements (Fig. 2(b)). The SBEM can calculate the heat flux and temperature at each node on the boundary. In order to accurately solve the internal flux distributions and conveniently performed the integration, the RVE is further discretized into a series of parametric sub-cells, as depicted in Fig. 2(c). The coordinate mapping relationship is shown in Fig. 2(d), where the four-node isoperimetric element is a typical internal parametric sub-cell. For the kth kth sub-cell, the node mapping relationship between the coordinate system $\left(y_2, y_3\right)$ and the reference coordinate system $\left(\xi, \eta\right)$ is as follows [36]:

$$y_i(\eta,\xi) = \sum_{f=1}^{4} N_f(\eta,\xi)y_i^{(f,k)}, i = 2,3 \tag{43}$$

where $f = 1,2,3,4$ and $f+1 \to 1$ when $f = 4$. The superscript k represents the number of quadrilateral sub-cells. The coordinates ξ and η range from -1 to 1. In the coordinate system, the shape function can be written as a function of the node coordinates, that is:

$$N_1(\eta,\xi)=\frac{1}{4}(1-\eta)(1-\xi), N_2(\eta,\xi)=\frac{1}{4}(1+\eta)(1-\xi)$$
$$N_3(\eta,\xi)=\frac{1}{4}(1+\eta)(1+\xi), N_4(\eta,\xi)=\frac{1}{4}(1-\eta)(1+\xi) \tag{44}$$

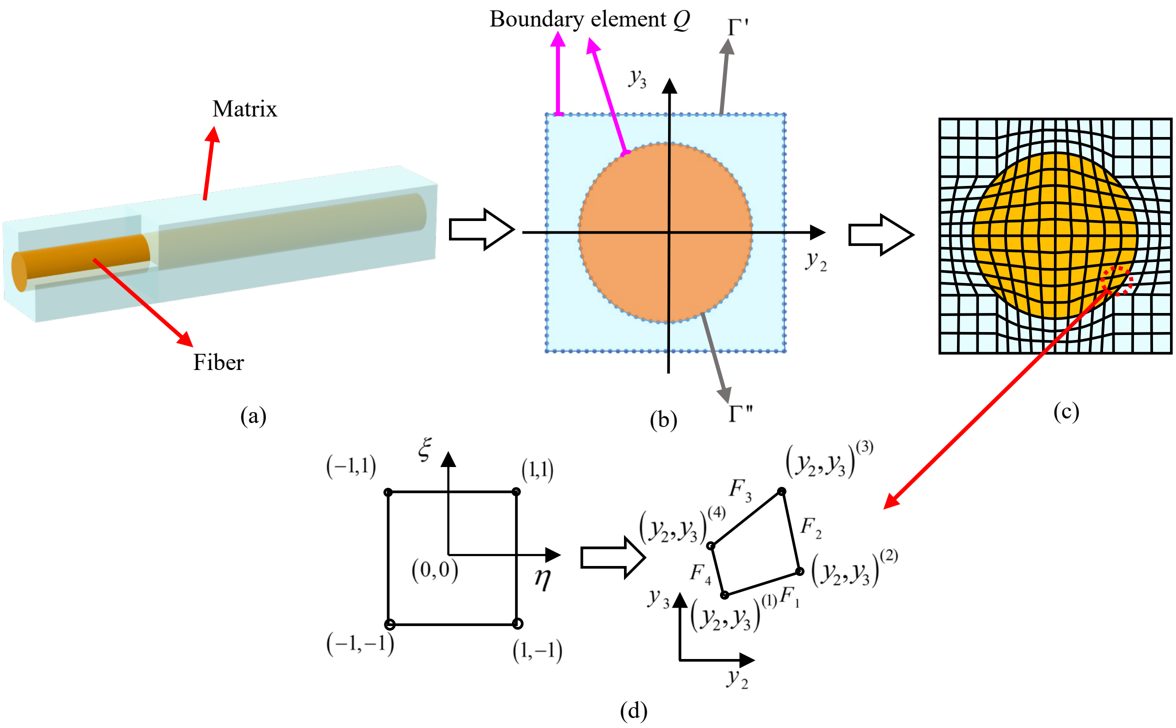

Fig. 2. Microscopic modeling scheme of the continuous FRCs: (a) 3D RVE, (b) Discretized boundary, (c) Discretized RVE with parametric sub-cells, (d) Mapping relation between the reference coordinate system and the actual coordinate system.

3. Thermal conductivity of unidirectional FRC

The mixing rate formula has been proved to be an effective method to predict the longitudinal thermal conductivity with a high accuracy [37]. The investigation of transverse thermal conductivity has attracted more attention due to the influence of the non-uniform material properties and geometric shapes, which exhibit periodical variations. Herein transverse thermal conductivity of unidirectional composites is investigated.

3.1. Thermal conductivity of composites with different fiber content

To study the influence of fiber volume fraction (FVF) on the transverse thermal conductivity, carbon FRC and glass FRC are both considered. The constituent material parameters are shown in Table l, where K_f and K_m represent transverse thermal conductivity of the matrix and the fibers, respectively. FVF of 0.2 ~ 0.7 with an interval of 0.05 are considered. To verify the proposed method, numerical results obtained from FEM and the experimental tests are compared [38] in Fig. 3. From the numerical results, it can be seen that the transverse thermal conductivity increases exponentially with the increase of FVF. In addition, it can be observed that the numerical results from the SBEM show good consistency with the experimental data, and is closer to the experimental results than the

FEM results.

Table 1

Thermal conductivity parameters of the constituent materials.

Materials	Transverse thermal conductivity $K\left(W \cdot m^{-1}K^{-1}\right)$	
	K_f	K_m
Carbon FRCs	66.6	0.1
Glass FRCs	1.06	0.24

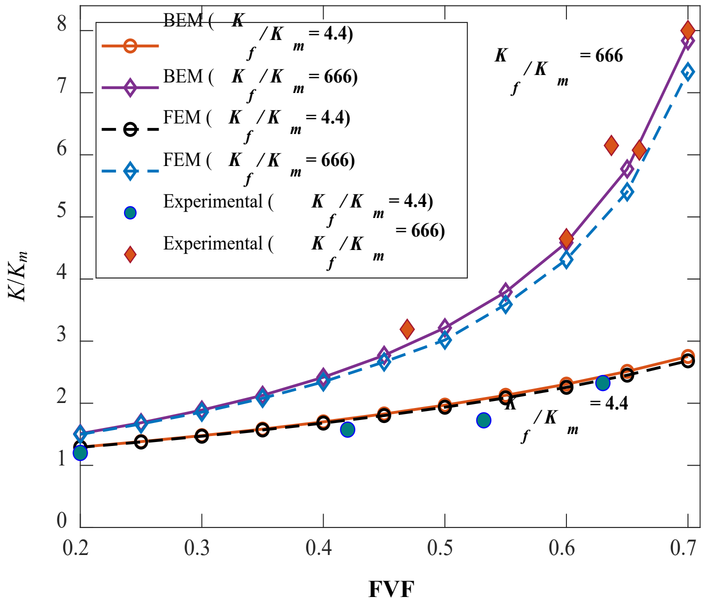

Fig. 3. The relationship between the FVF and transverse thermal conductivity.

3.2. Local temperature and heat flux analysis

Consider a glass FRC with a FVF of 0.45. A transverse temperature gradient of $1℃/m$ is applied on the RVE, where the temperature on the left- and right-hand sides of the RVE boundaries are -0.5℃ and 0.5℃, respectively. The numerical results of the local heat flux and local temperature distributions are shown in Fig. 4. For comparisons, the numerical results obtained by the FEM are also shown in the figure. The local heat flux fields predicted by the two methods agree with each other well. In addition, from the obtained heat flux and the temperature on the RVE boundary, the SBEM can analytically compute the heat flux of an arbitrary point in the domain, which makes it more convenient to study the heat flux of any region of interest.

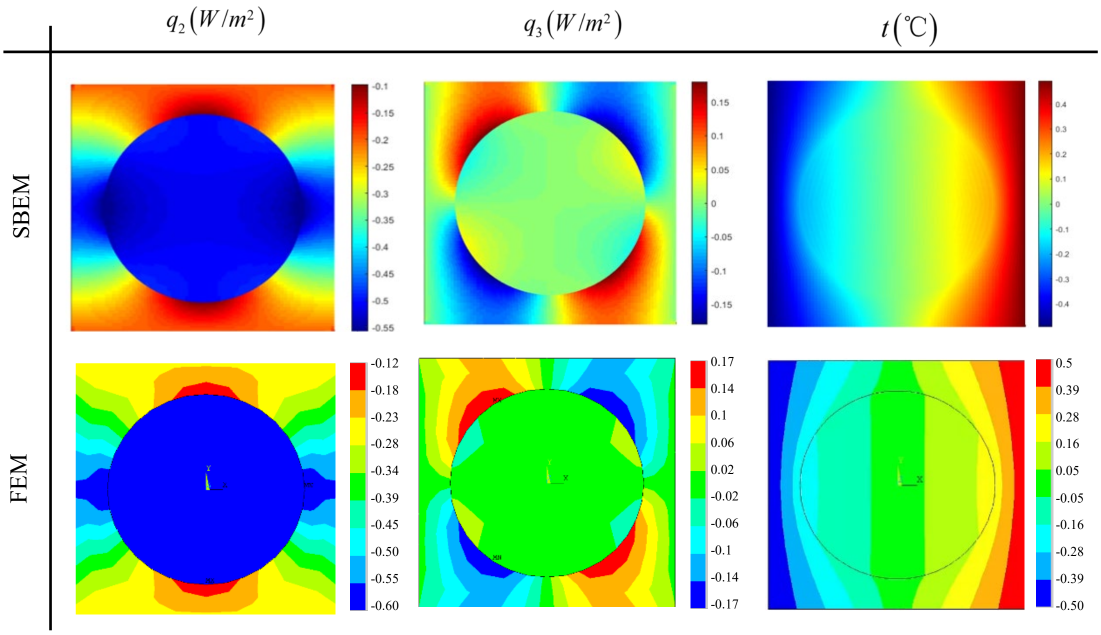

Fig. 4. Local flux and temperature comparisons between the FEM and the proposed SBEM under transverse grad $t = 1℃/m$.

To further investigate the influences of FVF on the heat flux, three different fiber contents are considered in Fig. 5. It can be found that there is a significant increase in the local heat flux within the RVE as the FVF increases. In addition, a concentration of heat flux is clearly observed at the interface region, indicating an uneven distribution and notable heat accumulation between the matrix and the fiber. Consequently, this non-uniform heat flux distribution may result in microscopic thermal damage on the interface. The patterns of the flux distribution are similar to those from other studies [33, 39], since the same principle of the homogenization procedure is followed, and similar geometry of the selected RVE are used.

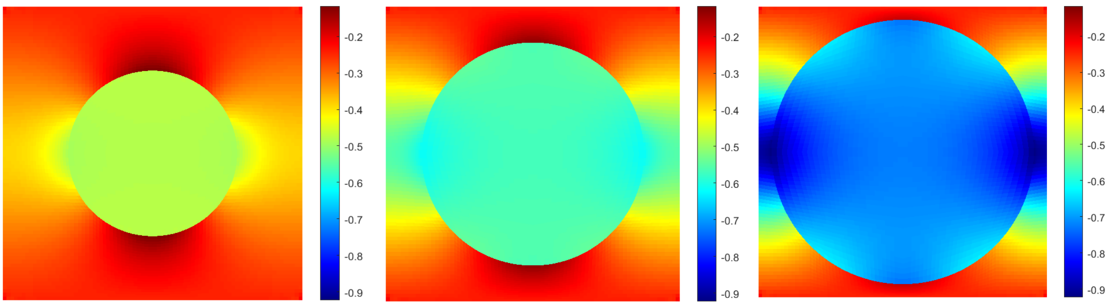

(a) (b) (c)

Fig. 5. Local flux distribution with consideration of FVF: (a) FVF=25%, (b) FVF=45%, (c) FVF=65%.

3.3. Temperature/flux distribution on the interface

To calculate the temperature and flux distributions with high accuracy, the circumferential interface is averagely discretized into 360 elements. FVFs of 0.35, 0.45 and 0.55 are considered, respectively, and the numerical results are shown in Fig. 6. It should be noted that some interface nodes are hidden deliberately for better display of the nodal information. Fig. 6 (a) illustrates the temperature distribution on the interface. It can be seen that the temperature profile, with consideration of the FVF, is smooth and continuous. Fig. 6 (b) and Fig. 6 (c), which depict the heat flux components on the interface along the y_2- and y_3-directions, respectively. Under the same temperature gradient conditions, the variation range of the temperature and the heat flux on the interface are sensitive to the FVF. An increase in the FVF can significantly increase the variation range of the temperature and heat flux. This means that volume fraction plays an important role in influencing local response, especially in the y_2- direction, which is the main direction of heat conduction.

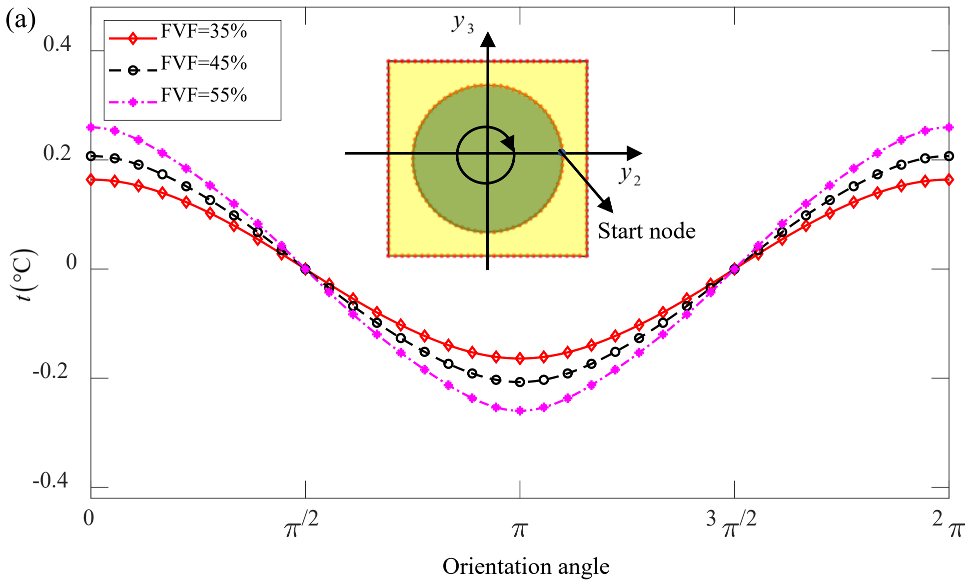

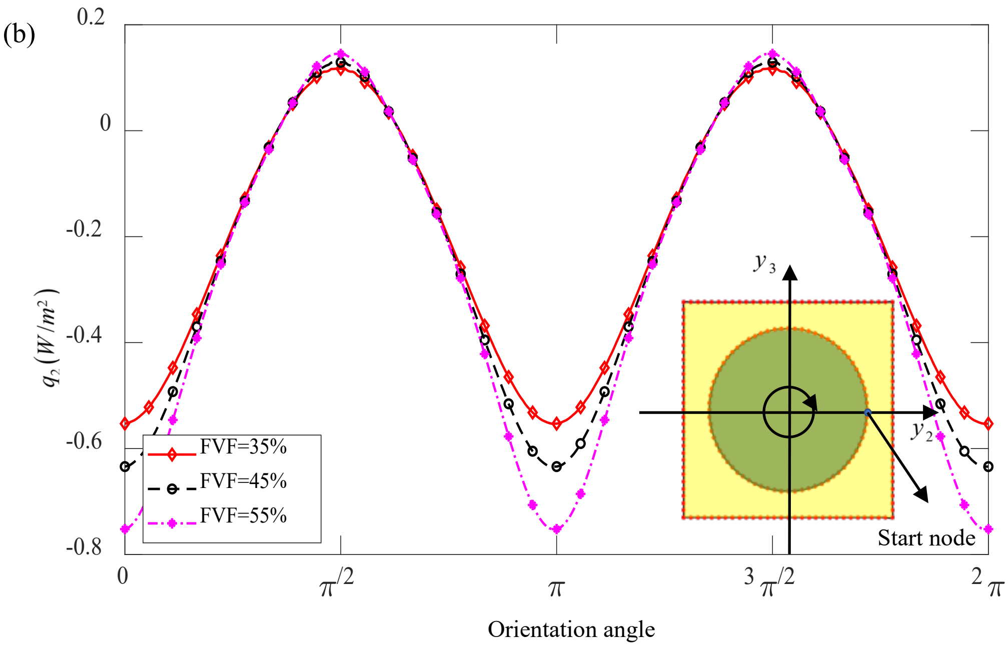

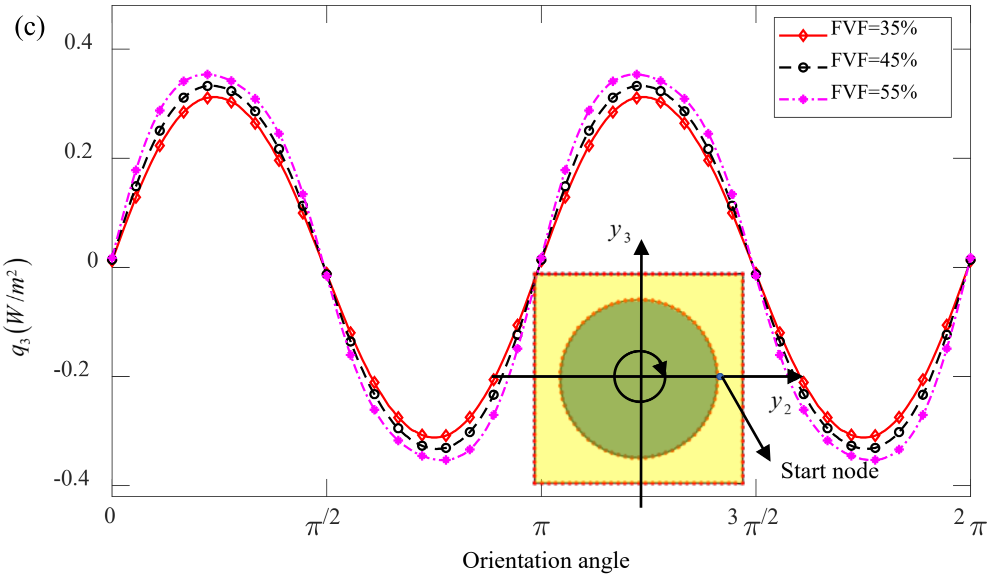

Fig. 6. Temperature and flux variations on the interface: (a) temperature t, (b) q_2, (c) q_3.

4. Influences of interface defect on the effective thermal conductivity

In the preparation process of a composite, some stochastic defects (pores or microcracks) are prone to occur at the interface [40] and potentially influence the properties of the composite. Due to the fact that the thickness of microcracks is much smaller than the size of pores, their effect on material thermal conductivity is relatively limited [41]. In view of this, this study only focuses on pores with clear thickness characteristics as representatives of interface defects. To evaluate the influences of interface defects on the thermal conductivity, the position, length and thickness of the defects are taken into consideration.

4.1. Modeling and analysis

4.1.1. Interface defect modeling

To accurately describe the defects on the circumferential interface, a parameter p is introduced, which is the ratio of the total length of interface defects to the entire circumferential interface length. As shown in Fig. 7, the central circular and the surrounding area are the fiber and matrix, respectively. The shaded regions surrounding the fiber are the interface defects between the fiber and the matrix. The defect thickness t is defined by the dimensionless parameter t/r, where r is the fiber radius. Thus, $0 \le p \le 1$, where $p = 1$ indicates that a fiber is completely detached from the surrounding matrix, while $p = 0$ denotes that the interface between a fiber and the surrounding matrix is perfect.

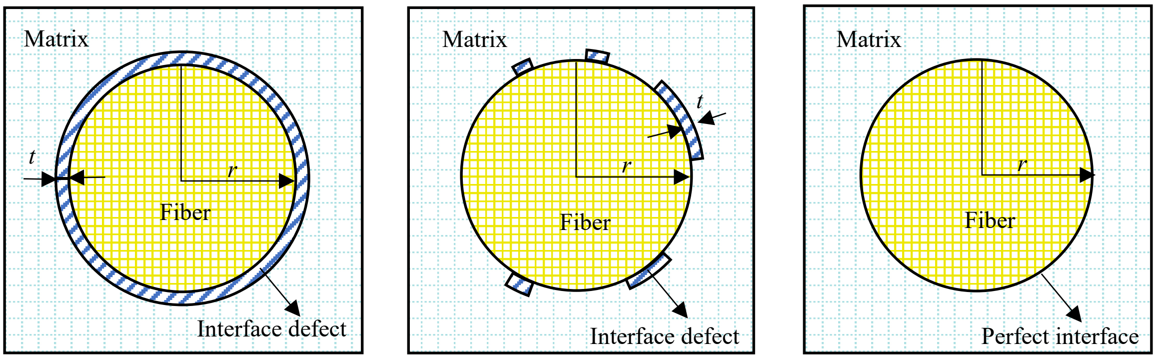

(a) $p=1$ (b) $0<p<1$ (c) $p=0$

Fig. 7. Interface defects between fiber and matrix in composites: (a) $p=1$, (b) $0<p<1$,(c) $p=0$.

During the numerical simulation by the SBEM, the node decoupling technique is used to simulate the interface defects. When a perfect interface is considered, the elements of the fiber and the matrix share a common node, e.g., A or B, as shown in Fig. 8(a). However, when interfacial damage is taken into account, as shown in Fig. 8(b), the node pairs B^+-B^- and A^+-A^- are positioned at the same coordinates on the interface, belonging to the subdomains on both sides of the interface. Herein the inner nodes A^- and B^- are the fiber nodes, and the outer nodes A^+ and B^+ are the matrix nodes. Interface defect is also considered as an air gap, assuming it possesses a thermal conductivity value of $0.026\left(W\cdot m^{-1}K^{-1}\right)$ [5].

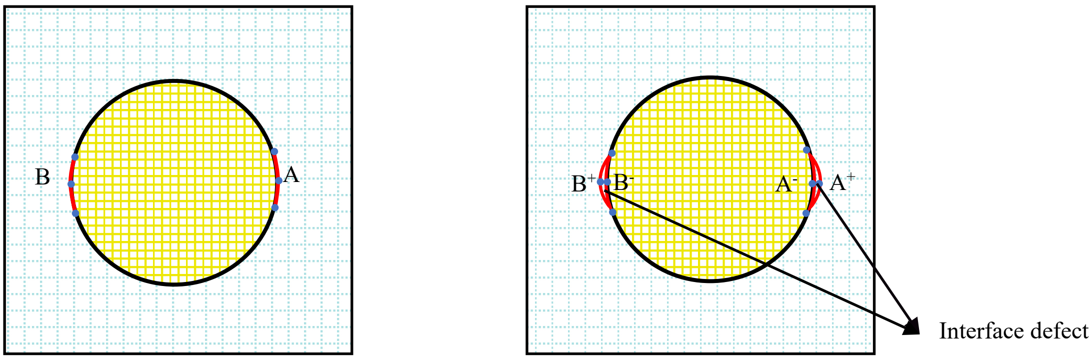

(a) (b)

Fig. 8. Node pairs at the interface: (a) Coupled node pairs, (b) Uncoupled node pairs.

The method presented by Hasselman [27] is used to quantify the influence of defects on thermal conductivity by introducing an equivalent contact thermal resistance. The presence of contact thermal resistance results in a temperature difference between the fiber boundary and the matrix boundary, which is ultimately reflected by the temperature difference of the interface nodes. In other words, interface nodes A^+ and A^- have different temperature. However, the heat flux of the fiber phase and the matrix phase at the same interface node remains equal. The mathematical equations are as follows:

$$-n_f\left(-k_f\nabla T_f\right)=k_c\frac{T_m-T_f}{t} \tag{45}$$

$$-n_m\left(-k_m \nabla T_m\right)=k_c \frac{T_f-T_m}{t} \tag{46}$$

where, n_f and n_m are the normal vectors of the fiber and matrix on the interface, respectively. k_f, k_m and k_c are the thermal conductivity of the fiber, matrix, and air, respectively. ∇T_f and ∇T_m denote the respective temperature gradients within the fiber and the matrix. t is the thickness of the interface defect.

4.1.2 Numerical analysis

To evaluate the influences of the interface defects, an RVE model containing interface defects with $t/r=0.025$ and $p=45/360=12.5\%$ is selected in the simulation. The position of a defect on the circumference interface can be defined in a polar coordinate system with the fiber center being the origin, where the endpoints A and B of the defect are shown in Fig. 9(a). As shown in Fig. 4 and Fig. 5 and Fig. 6, the heat flux concentration appears near the 0° position of the interface and decreases sharply along the interface from 0 degrees to the other end at $\pi/4$ position. The impact of interface defects located in this region on heat flux and temperature deserves further study. To this end, the ends at 0° and $\pi/4$ are labeled as points B and A, respectively in the following discussion. The influence of this interface defect on the local heat flux and temperature field are investigated. The simulation results of the local heat flux are shown in Fig. 9(b-c). For comparisons, a finite element model is developed in this paper with interfacial defects located on the matrix side of the interface. The interfaces are modelled by a third-phase material that has the material properties of air. The position, length, and thickness of the defect are the same as those used in the boundary element model. The numerical results obtained are also shown in the figure. It can be seen that the local heat flux fields predicted by the two methods agree with each other well. The heat flux shows significant changes along the y_2- and y_3-directions near the defect. In other words, the presence of the interface defect results in heat flux concentration and heat accumulation. Consequently, the effective thermal conductivity is affected.

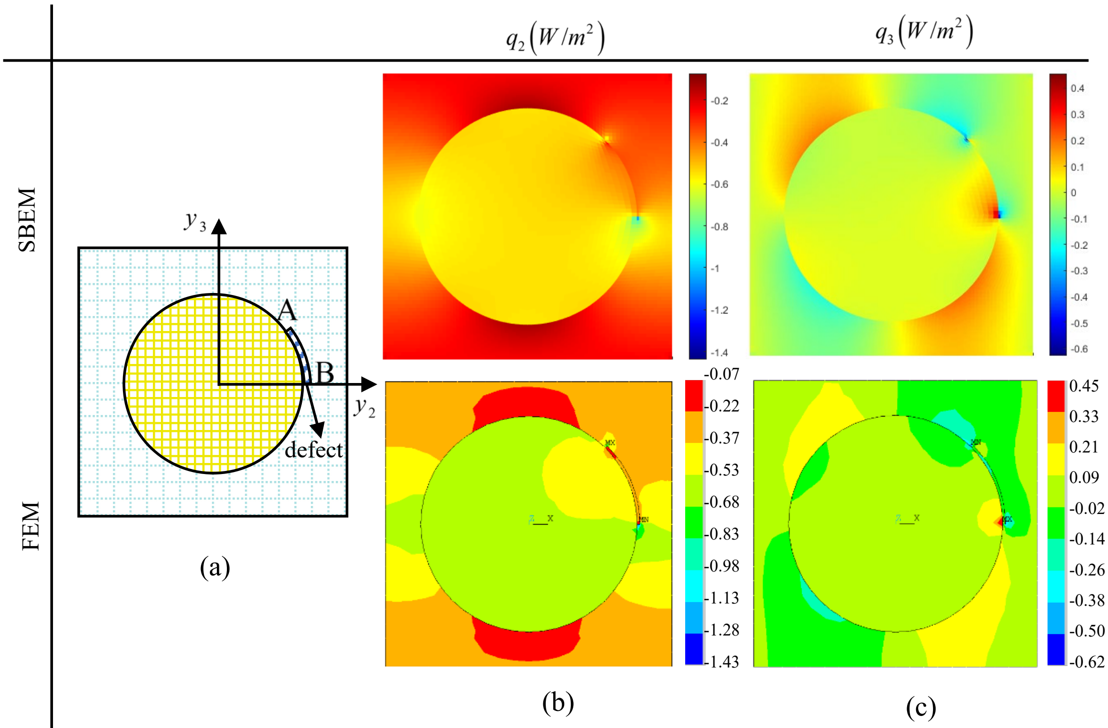

Fig. 9. Local flux distribution of model with interface defects comparisons between the FEM and the proposed SBEM under transverse grad $t = 1℃/m$.

The simulation results of the local temperature distribution are shown in Fig. 10(b, c). Due to the relatively large temperature difference of the background, the influence of interface defects shown in Fig. 10(b) is not significant compared to the perfect interface (Fig. 4). Therefore, a distribution map of the temperature fields of the two is presented, as shown in Fig.10(c). It can be clearly seen from Fig.10 that the interface defects hinder the heat transfer, resulting in different temperatures on the two sides of the defect (Fig.10(c)). The temperatures on the immediate right- and left-hand sides are higher and lower, respectively, than the temperatures of the same positions of the interface without the defect. The maximum temperature difference is $0.073^{\circ}C$ and located at the center of the defect.

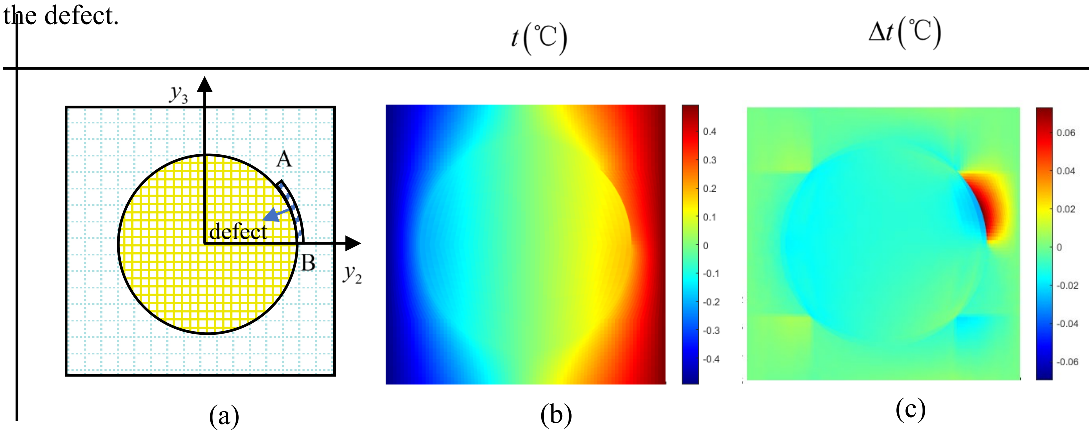

Fig. 10. Local temperature distribution of model with interface defects.

The temperature and heat flux profiles of the matrix along the interface with a defect are shown in Fig. 11. The simulation results show a significant change in the temperature and flux in the defect area. From Fig. 11(a), it can be seen that the presence of the interface defect causes a notable increase in the temperature within the defect area. This is attributable to that the interface defects hinder the normal heat flow, resulting in a local temperature increase and local heat flux decrease within this region. The heat flux in Figs. 11(b)-(c) shows abrupt changes at both ends of the defect. Notably, it can be seen in Fig. 11(b) that the abrupt change in the heat flux at point B is greater than that at point A. More specifically, the heat flux q_2 jumps from $-0.19W/m^2$ to $-0.527W/m^2$ at point A, and drops from $-0.40W/m^2$ to $-1.69W/m^2$ at point B. The existence of defects leads to a concentration of heat flux at both tips of the defect, and the degree of concentration is related to the location of the defect tips. If a defect tip appears in a region where interfacial heat flux is high, the degree of heat flux concentration is more intensive. The abrupt change is also observed in Fig. 11(c) for q_3 at both ends of the interface defect.

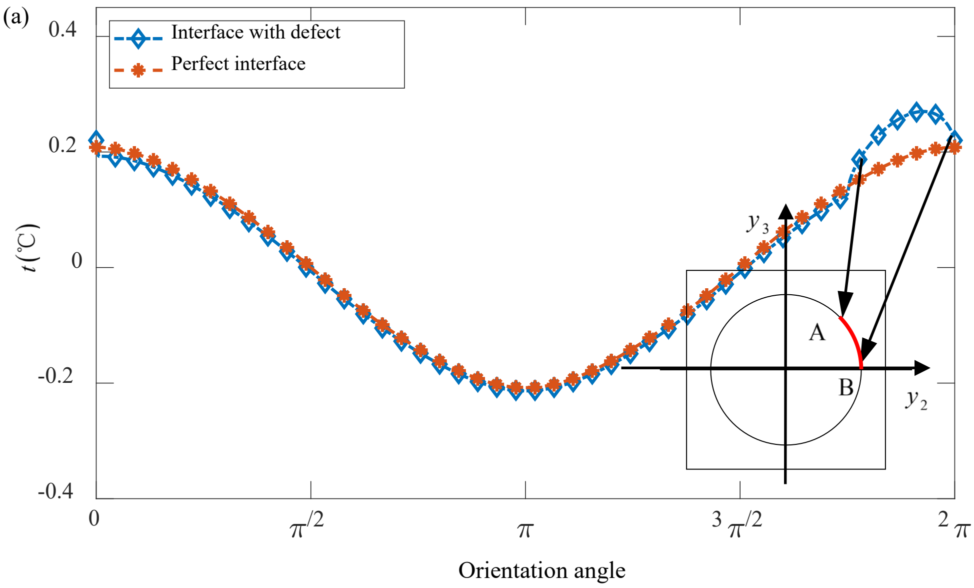

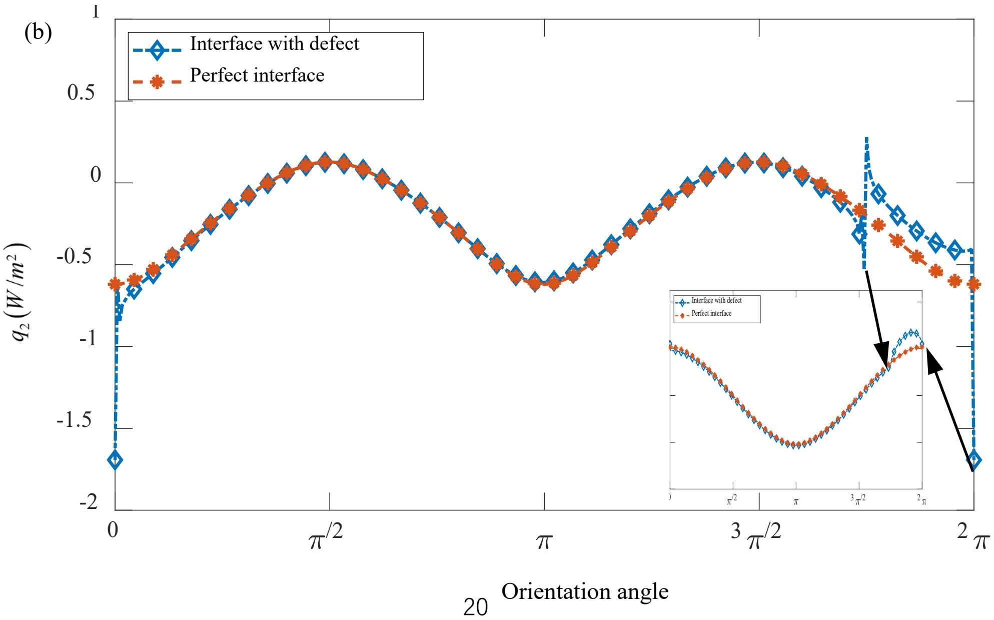

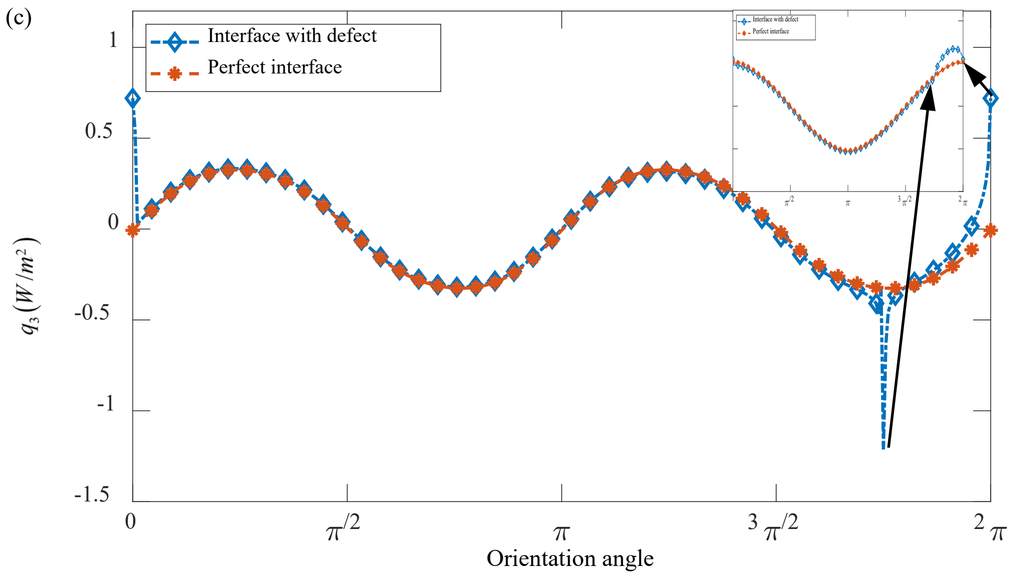

Fig. 11. Temperature and heat flux distributions on the interface: (a) t ,(b) q_2 ,(c) q_3 .

4.1.3. The effects of stochastic defect on heat flux

By using the proposed SBEM, the effective thermal conductivity of the FRC with consideration of interface defects can be evaluated. Herein, the influences of defect length, thickness and position on the thermal conductivity are further investigated. Fig. 12 shows four RVEs with defects of identical thickness and total defect length that are randomly distributed along the interface. The total defect length is $p = 50\%$ and the thickness is $t/r = 0.15$. Fig. 12 shows the defect distributions of the four RVEs and their respective distributions of q_2. The calculated values of the effective thermal conductivity considering the different positions of interface defects are $0.3912 W \cdot m^{-1}K^{-1}$, $0.4092 W \cdot m^{-1}K^{-1}$, $0.4157 W \cdot m^{-1}K^{-1}$ and $0.4273 W \cdot m^{-1}K^{-1}$, respectively.

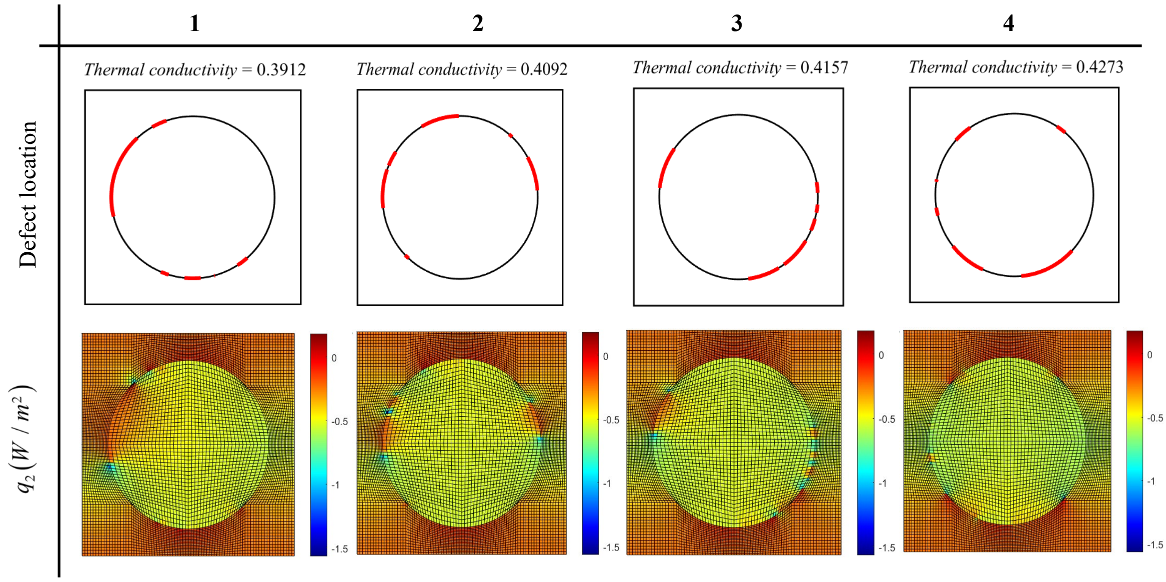

Fig. 12. Local flux distributions in the RVE with interface defect.

4.2 The influence of interface defect location on the effective thermal conductivity

4.2.1 The location of interface defect along the circumference

The interface defect in the RVE of length $p = 8.33\%$, thickness $t/r = 0.1$ is chosen to study the effect of defect location on the thermal conductivity. The location of a defect along the circumference interface is defined by the position of the middle point of the defect, i.e., by the angle θ in the polar coordinates. The effective thermal conductivity of the RVE having defects at various positions is calculated, and compared with that of the RVE with perfect interface, as shown in Fig. 13. It is shown clearly that the location of the interface defect has a significant effect on the effective thermal conductivity. When the defect is located at 0 or π, the equivalent thermal conductivity is the minimum. When the defect is at $\pi/2$ or $3\pi/2$, the equivalent thermal conductivity is almost the same as that of the perfect interface. This suggests that the smaller the angle between the radial direction of the defect center and the direction of heat conduction, the greater the impact of interface defects on heat conduction.

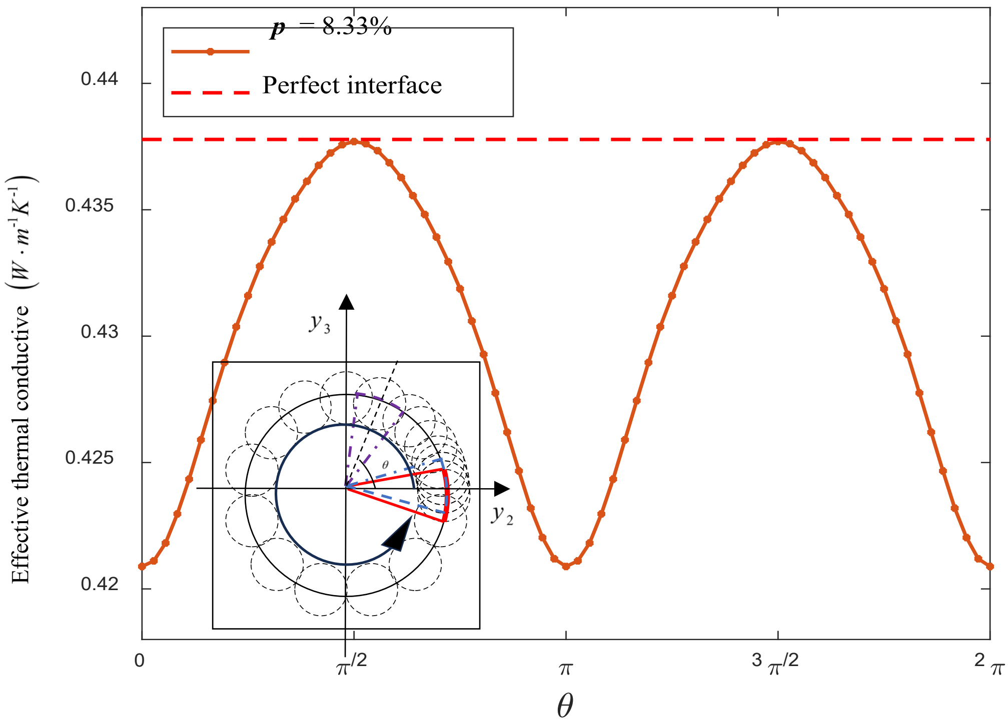

Fig. 13. The relationship between the interface defect location and effective thermal conductive.

4.2.2 Randomly distributed interface defects along the circumference

In the real situation, a composite may contain many fibers with interface defect randomly distributed along fiber circumferences. The influence of the interface defects on the effective thermal conductivity needs to be assessed statistically. In this paper, the Von Mises distribution is used to describe the position of circumferential defects. The probability density function of the Von Mises distribution can be expressed as:

$$f(\theta \mid \mu, \kappa) = \frac{e^{\kappa \cos(\theta - \mu)}}{2\pi I_0(\kappa)} \tag{47}$$

This formula describes how the probability density of an angle θ on the unit circle varies with its proximity to the mean direction μ and as a function of the concentration parameter k, which governs the degree of clustering around the mean. Where, θ is an angle within the range of $[0,2\pi]$. μ is the mean of the distribution and is also an angle within the range of $[0,2\pi]$. κ is the concentration parameter of the distribution, which is a non-negative real number. When $\kappa=0$, it represents a uniform distribution. $I_0(\kappa)$ is the modified Bessel function of the first kind.

RVEs of fixed interface defect length of $p=10\%$, $t/r=0.1$ are considered. There are 36 identical defects randomly distributed along the interface. In the polar coordinates, starting from 0, the mean value μ of the Von Mises distribution of interface defects are set at every $\pi/4$ interval for the different position. The parameter κ is set as $\kappa=0,3.0,6.0,10.0$ for different concentration. Five hundred Monte Carlo simulations are conducted for each combination of the distribution parameters to obtain RVEs samples featuring interface defects at varying locations along the interface. Subsequently, the effective thermal conductivity of each of the samples is calculated, and the results are presented in Fig.14, wherein the horizontal axis denotes the mean (μ) value of the angular (position) distributions, and the vertical axis denotes the expected value of the effective thermal conductivity of the distributions. It is evident that when the concentration is higher (κ value is large), the μ has a significant impact on the thermal conductivity coefficient. When μ is at 0 and π, the equivalent thermal conductivity reaches its minimum value, and at $\pi/2$ and $3\pi/2$, it reaches the maximum value. However, when the concentration is poor (κ value is small), the impact of position on the thermal conductivity becomes less significant. As κ approaches 0, i.e., the distribution of interface defects around the circumference of the fiber tends to be uniform, the effective thermal conductivity approaches $0.4368\left(W\cdot m^{-1}K^{-1}\right)$. This observation suggests that when the number of defects on an interface is sufficiently large, the thermal conductivity can be considered independent of the position of the individual interface defects.

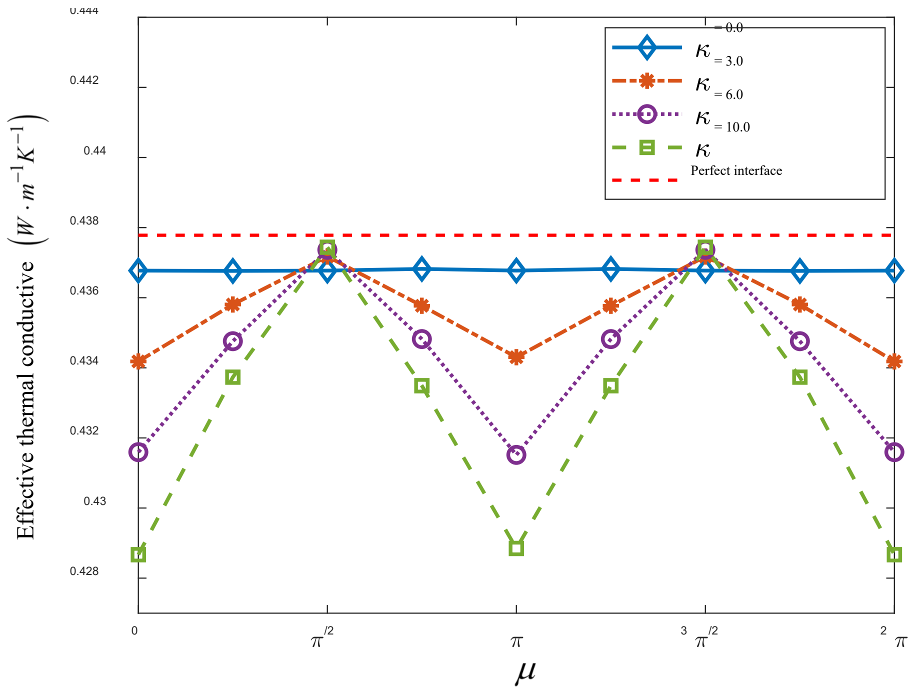

Fig. 14. The relationship between the interface defect location and effective thermal conductive under different concentration κ

4.3. Effect of stochastic interface defects on the effective thermal conductivity

The microstructure of a composite with random interface defects can be characterized by a random unit cell w^s. Assuming that a unit cell contains I randomly distributed interface defects, the set of all defects in this random cell can be defined as:

$$w^s = \left(\delta_1^s, \delta_2^s, \cdots \delta_I^s\right) \tag{48}$$

where one defect is represented by the following parameters:

$$\delta = (\theta, p, t) \tag{49}$$

Thus, the thermal conductivity of the composite material with random interface defects is an oscillation function related to the random variable w^s, and the effective thermal conductivity tensor is defined as [42]:

$$k_{ij}^H\left(w^s\right) = \frac{1}{|Y|}\int_Y \left(k_{ij}\left(\boldsymbol{y}, w^s\right) + k_{iq}\left(\boldsymbol{y}, w^s\right)\frac{\partial \chi^j\left(\boldsymbol{y}, w^s\right)}{\partial y_q}\right) dY \tag{50}$$

The probabilistic moments of the effective thermal conductivity are obtained using the statistical estimation methods, from which the expected effective thermal conductivity tensor is calculated as:

$$E\left[k_{ij}^H\right] = \frac{1}{M}\sum_t^M k_{ij}^{Ht} \tag{51}$$

where $k_{ij}^{Ht}\left(w^s\right), t = 1, \cdots, M$ are given series of the randomly generally tensor components.

To effectively investigate the effect of the stochastic interface defects, the Monte Carlo method is implemented into the SBEM. A RVE model with stochastic interface defects is taken as an example to calculate the effective thermal conductivity. The entire circular interface of the RVE is discretized into 360 boundary elements, the nodes of some of which are decoupled to represent the interface defects with specified length. For instance, if a defect extends across E consecutive elements on the circular interface, $E-1$ internal nodes of the elements are decoupled. With full consideration of their randomness, these defects can be generated by using a random function within the range of $\left[0^{\circ},360^{\circ}\right]$. The impact of stochastic interface defects on the effective thermal conductivity of the FRC is then studied by varying the total defect length and thickness in the simulation. Fig. 15(a) is the Quantile-Quantile (Q-Q) plot, which confirms the predictions approximately follow a normal distribution as,

$$X \sim N\left(\mu,\sigma^{2}\right) \tag{52}$$

where X represents the effective thermal conductivity. The parameter μ is the mean of the predictions with full consideration of different random variables. The variance σ^{2} indicates the degree of deviation from the mathematical expectation.

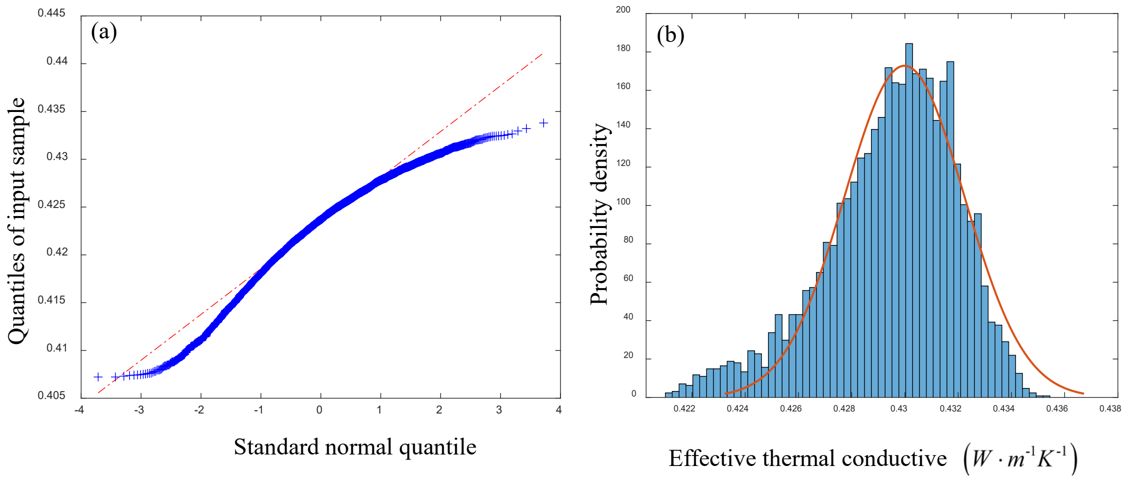

Fig. 15. Probability distribution with 5000 specimens: (a) Q-Q plot, (b) A comparison between statistical results and fitting results.

4.4. Determine the appropriate sample size

The sample size plays a significant role in determining the calculation accuracy during the numerical calculation by utilizing the Monte Carlo method. Considering the calculation accuracy and computational efficiency, 10 sets of samples. i.e., 200, 500, 800, 1000, 1200, 1600, 2000, 2500, 3500, and 5000, are selected for determining an appropriate sample size. The dimensionless interface defect thickness t/r and the defect length p are, respectively, 0.01 and 33.33%. Table 2 shows the predicted thermal conductivity using the selected samples, which clearly indicates that using over 800 samples has virtually the same degree of accuracy.

Table 2

Convergence trend of different specimen numbers

Sample number	The mean of effective thermal conductivity coefficient $\left(W\cdot m^{-1}K^{-1}\right)$	Variance

200	0.4242	3.4E-5
500	0.4242	3.1E-5
800	0.4241	2.7E-5
1000	0.4241	2.5E-5
1200	0.4241	2.6E-5
1600	0.4241	2.8E-5
2000	0.4241	2.8E-5
2500	0.4241	2.7E-5
3500	0.4241	2.7E-5
5000	0.4241	2.7E-5

To study the distribution of each of the group using frequency density histograms and probability density function curves, the statistical grouping method proposed by Freedman and Diaconis [43] is used in the data sorting. Based on the distance between the upper limit b and lower limit a of the calculated thermal conductivity, the results of all the samples are divided into 30 groups, thus, the class interval Δ is $\Delta = \frac{b-a}{30}$. The shaded area in the frequency density histogram of Fig. 16 (a) is the statistical frequency F of one interval. Correspondingly, the shaded area in the probability density function graph of Fig. 16 (b) is the statistical probability P of the same interval. Considering that the data has a normal distribution, thus,

$$P = \int_{\Delta} \frac{1}{\sqrt{2\pi}\sigma} e^{\left(-\frac{(x-\mu)^2}{2\sigma^2}\right)} d\Delta \tag{53}$$

The probability function is integrated over each of the interval Δ. With the obtained F and P, the difference of them can be calculated as the error function. For the ith interval Δ_i, the corresponding F_i, P_i, and the absolute error $\left|F_i - P_i\right|$ can be obtained, from which the average error $\overline{P}$ is calculated by:

$$\overline{P} = \frac{\sum_{i=1}^{30} \left|F_i - P_i\right|}{30} \quad (i = 1, 2, \cdots 30) \tag{54}$$

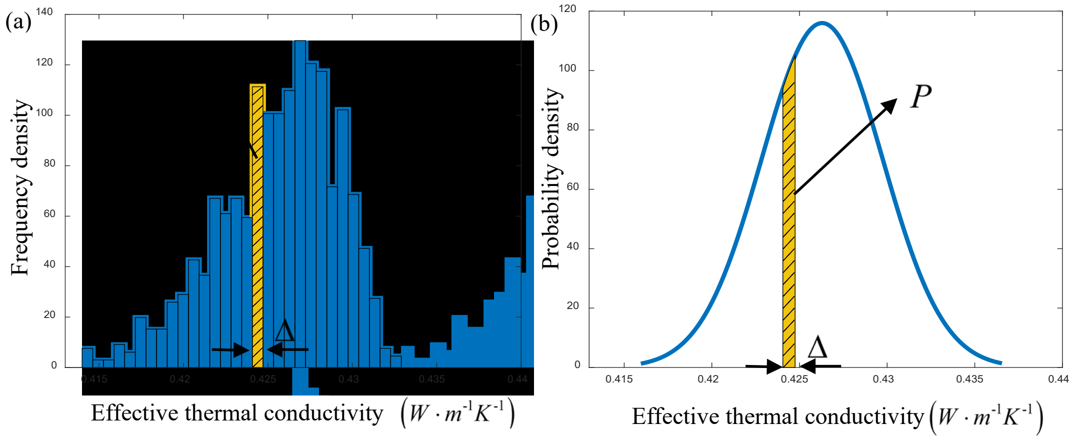

Fig. 16. Comparison between statistical results and fitting results: (a) Frequency density, (b) Probability density curve.

From the statistics, the error $\overline{P}$ will converge to a small value when the sample size is sufficiently larger. Fig. 17 shows the tendency of the calculated error $\overline{P}$ for each of the sample groups, which shows that the average error approaches and converges to 0.006 as the sample count surpasses 1000. To consider calculation accuracy and computational efficiency, 1000 is considered an appropriate sample size for this study.

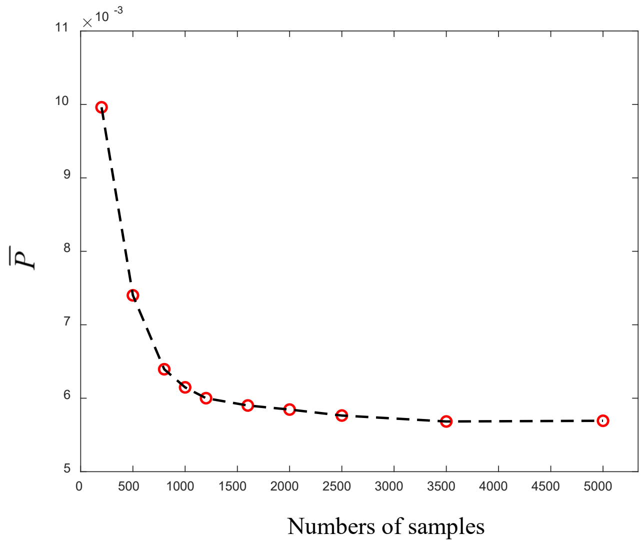

Fig. 17. Numerical results of the error with consideration of sample number.

4.5 The influencing factors of interface defects on thermal conductivity

4.5.1 Defect length

RVEs with a fixed defect thickness $t/r = 0.1$ and five different defect lengths, i.e., $p = 25\%$, 33.33%, 41.67%, 50% and 60%, are considered, respectively. The frequency density histogram and the probability density chart of the statistical results are presented in Fig. 18. It is evident that the defect length represents a notable impact on the effective thermal conductivity. Specifically, as the increase of the defect length, the mean of the effective thermal conductivity decreases from $0.431 W \cdot m^{-1} K^{-1}$ to $0.401 W \cdot m^{-1} K^{-1}$ with a change of the variance from 4.133E-6 to 7.022E-5.

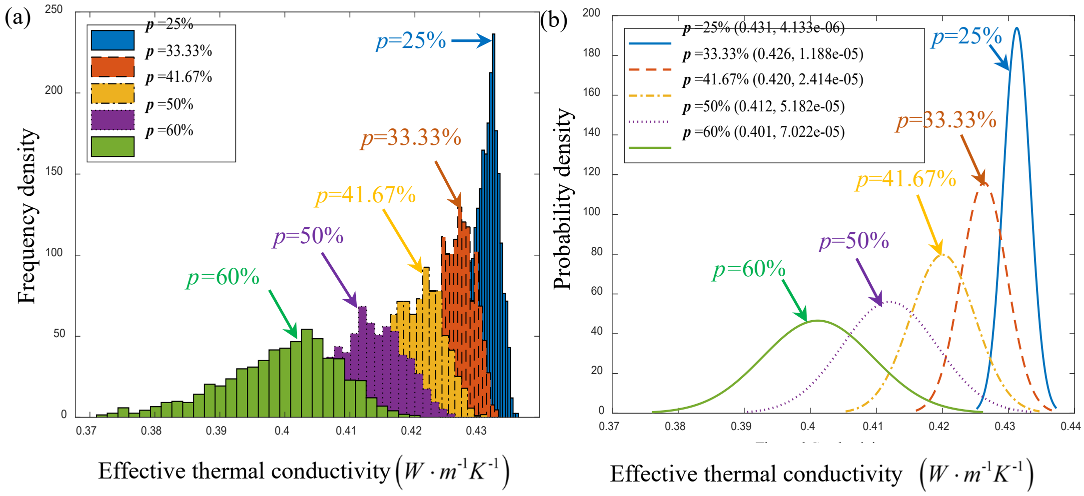

Fig. 18. $t/r = 0.1$, the relation between the multiple defect length and effective thermal conductive: (a) Frequency density, (b) Probability density.

To gain a deeper insight into the data distribution, a box plot is further featured in Fig. 19(a). This visual representation of the statistical data includes a series of essential indicators, including the median, minimum, and maximum values, the upper quartile and lower quartile, as well as the outlier data. Herein the thermal conductivity of the perfect interface is also depicted in the graph by using the red dashed lines for comparisons. It is evident that the median of effective thermal conductivity decreases with the increase of the defect length p. Moreover, the distribution range of the effective thermal conductivity is larger when the defect length p is greater. In addition, the presence of the outliers below the lower edge of the distribution range indicates that the overall data distribution represents a leftward skew. This skewness is attributed to the interface defects, which results in a reduction in thermal conductivity. The correlation between the mean value of the effective thermal conductivity (y) and the defect length (x) of the interface is shown in Fig. 19(b). The fitting equation derived from the numerical results can be written as:

$$y = -0.0906x + 0.455 \tag{55}$$

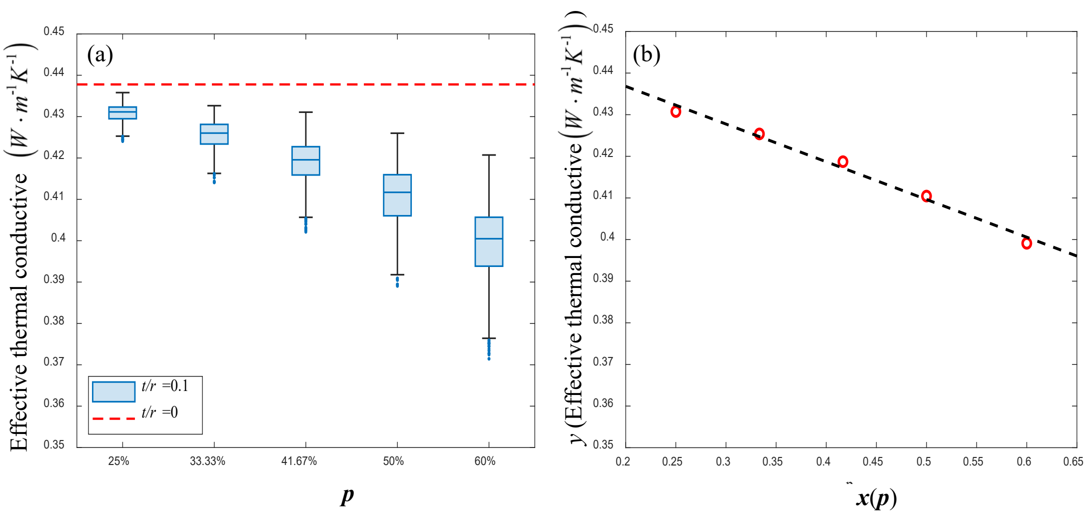

Fig. 19. Effective thermal conductivity with consideration of different defect lengths: (a) Box plot, (b) Data fitting curve.

In the heat conduction process, the interface serves as a heat transfer channel between the matrix and the fiber phase. However, interface defects always hinder the normal heat transfer process. The length and thickness of interface defects are two main factors that affect thermal conductivity. In this evaluation, the thickness of the interface defects is fixed, and the defect length changes. When the defect length is small, the influence of defect thickness is a dominating factor. Thus, the reduction in the effective thermal conductivity is relatively slow as the length increases. However, when the length exceeds a certain value (33.33%), the influence of defect length becomes the main factor. Thus, the reduction in the effective thermal conductivity is relatively fast as the length increases. In general, as the defect length increases, the effective thermal conductivity decreases approximately linearly.

4.5.2 Defect thickness

RVEs of fixed interface length $p = 33.33\%$ with five different interface defect thicknesses $t/r = 0.01,\ 0.05,\ 0.10,\ 0.15,\ 0.2$ are considered. The frequency histogram and probability density chart are shown in Fig. 20(a) and Fig. 20(b), respectively. It is evident that the thickness of the defects also plays a crucial role in determining the effective thermal conductivity. Similar to the analyses on the defect length, the effective thermal conductivity obviously decreases as the defect thickness increases, with an increasing variance.

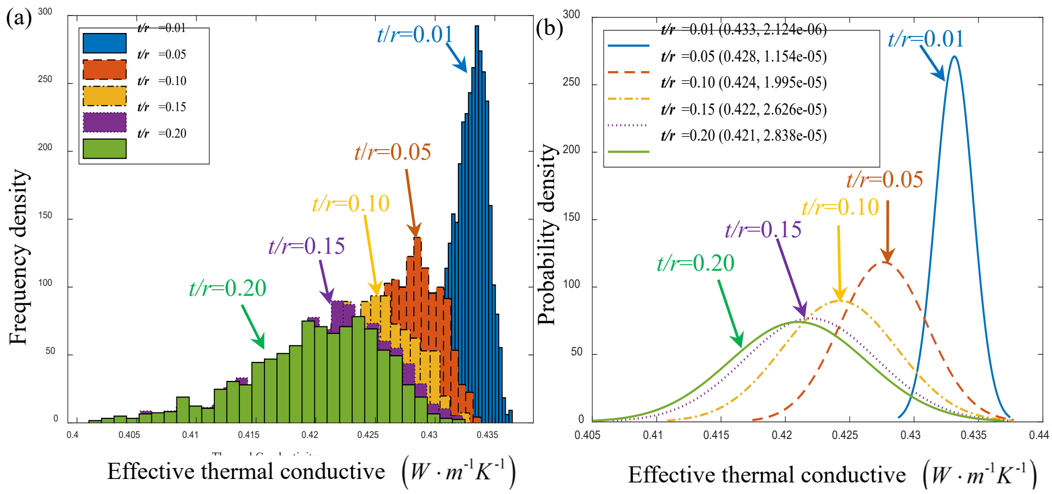

Fig. 20. $p = 0.33$, the relation between the multiple defects thickness and effective thermal conductive: (a) Frequency density, (b) Probability density.

Fig. 21(a) presents a box plot depicting the relationship between the interface defect thickness t/r and the thermal conductivity of the FRC with a fixed defect length. Herein the red dashed line represents the thermal conductivity of the FRC with perfect interface bonding. It is noticeable that the median of the effective thermal conductivity experiences a certain decrease as t/r increases. However, the downward trend gradually levels off. Once the defect thickness t/r reaches 0.15, the quartile difference (length of the box) for each group remains relatively constant, indicating a stabilization in the dispersion of the data. In addition, it is observed that the outliers are concentrated below the boundaries of the box plot, indicating that the overall data distribution is skewed towards the left-hand side since interface defects only reduce the thermal conductivity. Fig. 21(b) depicts the correlation between the mean value of the effective thermal conductivity (y) and the thickness (x) of the interface defect. In general, the relationship between the two is approximately linear. The fitting equation is as follows:

$$y = -0.0667x + 0.431 \tag{56}$$

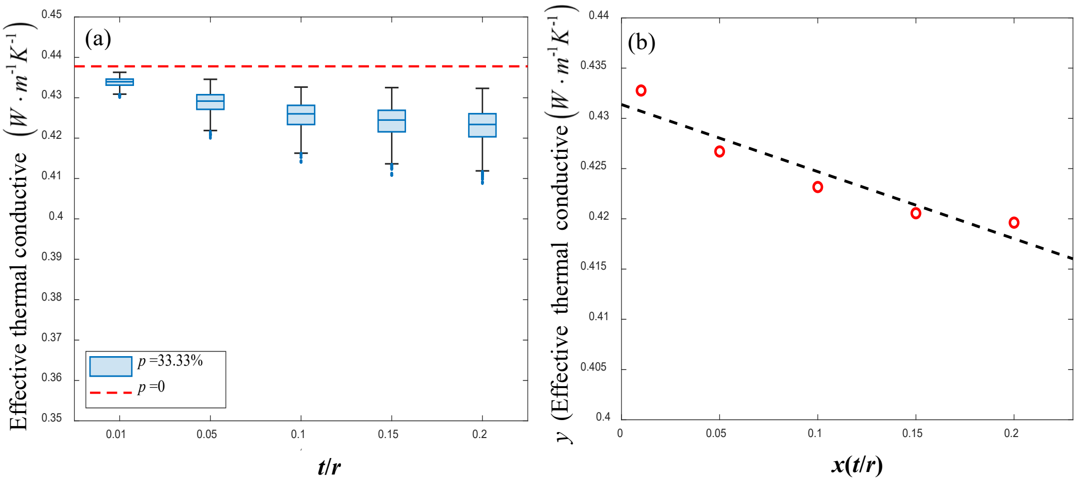

Fig. 21. Effective thermal conductivity of materials under multi defect thickness conditions: (a) Box plot, (b) Correlation function.

4.5.3. Area of Defect

When considering the influence of the area of interface defects on the thermal conductivity, Eq. (57) is proposed to take into account the arc length and the thickness of an interfacial defect. Fig. 22 shows the determination of the defect area that can be calculated as follows:

$$\begin{aligned} area &= \frac{n}{360} \times \pi \times t(t+2r) \\ &= p \times \pi \times t(t+2r) \end{aligned} \tag{57}$$

where the parameter, n, is the degree of the central angle relative to the dimensionless defect length p, and $p = \frac{n}{360}$.

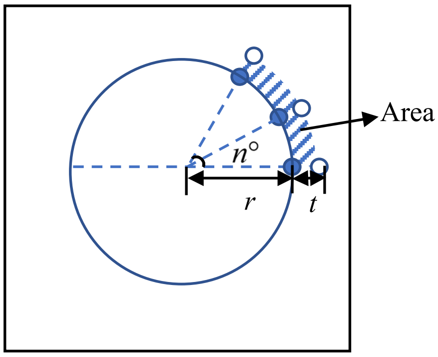

Fig. 22. The area of the interface defect.

The RVEs with interface defect areas 0.01, 0.02, 0.03, 0.04, 0.05, 0.06, 0.07, 0.08, 0.09, and 0.1 are considered, respectively, with variable defect length, p, and thickness, t. The defect length p is randomly chosen, and the defect thickness is calculated then from Eq. (57). The randomly chosen defect length and the calculated thickness are required to be smaller than their respective pre-defined maximum values, which is practically possible. Based on the maximum defect length, thickness and the given area, the minimum value of defect length and thickness can be determined. 1000 defect samples are generated for each of the above 10 defect areas by Monte Carlo experiments. The effective thermal conductivity of the samples is statistically analyzed, and the results are shown in Fig. 23.

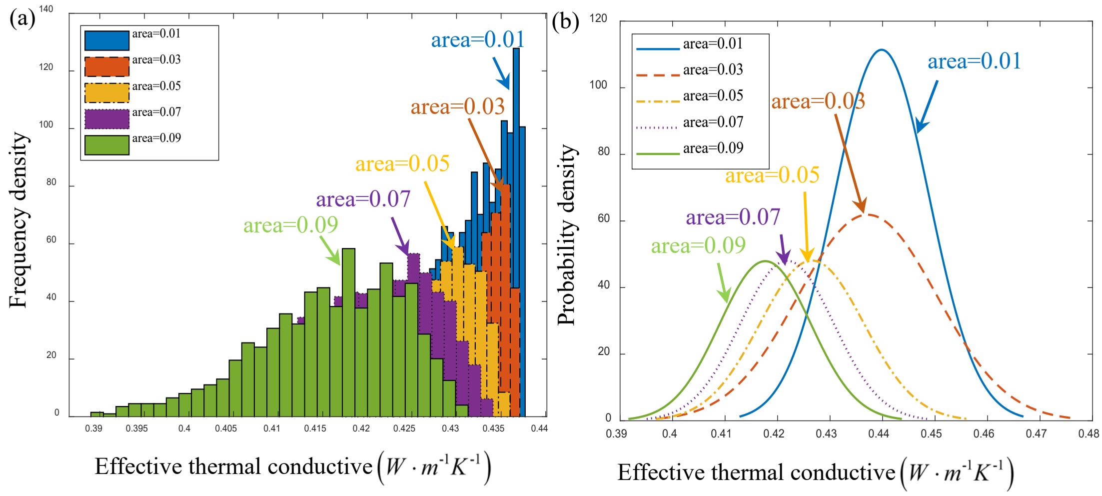

Fig. 23. FVF=45%, probability distribution of interface defect and effective thermal conductive under the condition of multiple defect areas: (a) Frequency density, (b) Probability density.

Fig. 24(a) presents a box plot depicting the effective thermal conductivity distributions. It is evident that the median effective thermal conductivity exhibits a uniform decreasing trend with the increase of the defect area. The correlation between the mean value of the effective thermal conductivities and the interface defect area is depicted in Fig. 24(b). It represents a strong linear correlation, and the fitting equation is expressed as:

$$y = -0.181x + 0.432 \tag{58}$$

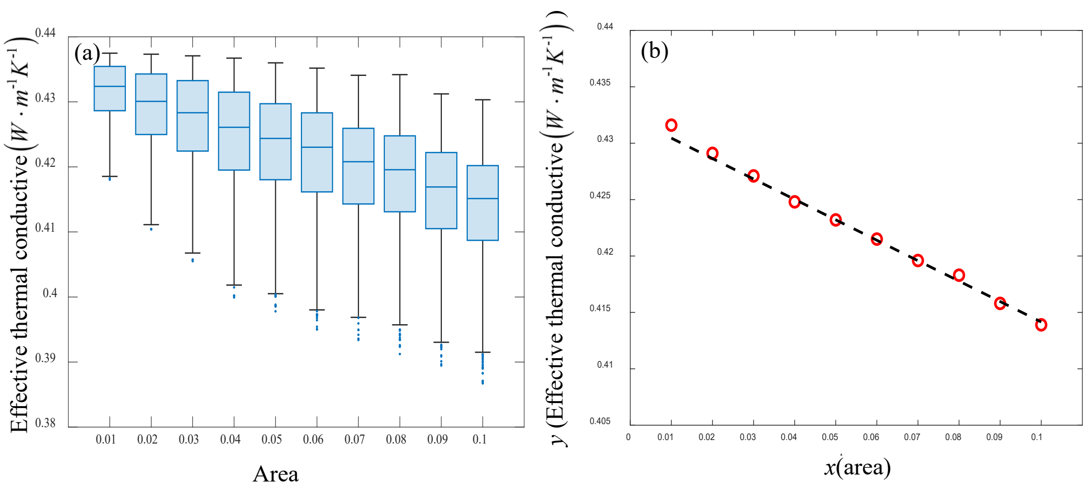

Fig. 24. Effective thermal conductivity with consideration of interface defect area: (a) Box plot, (b) Correlation function.

5. Conclusions

The present investigation proposes a new micromechanical model for the prediction of the effective thermal conductivity of FRC with full consideration of random interface defects. This study uses glass fiber-reinforced composite materials as the research object, but the method and computer program can be easily extended to other fiber-reinforced composite materials. Under the assumption that the material solely comprises interface defects, the model idealizes these defects as discontinuous circular arc-shaped segments distributed along the circumference of the interfaces. This approach facilitates a quantitative examination of how the length, thickness, and area of interface defects influence thermal conductivity. The effect of defects on thermal conductivity is quantified by introducing an equivalent contact thermal resistance. This method streamlines the complex heat transfer process at the contact interface but overlooks the true physical characteristics of the interface, which can similarly affect the accuracy of the predictions. It is noteworthy that the model developed herein is a two-dimensional RVE model, suitable only for investigating the impact of interface defects on transverse heat conduction. To analyze the axial thermal conductivity, the establishment of a three-dimensional RVE model is necessitated. In addition, the current model has not fully captured all the intricacies present in real materials, thereby potentially impacting the accuracy of predictions. The main conclusions of this study are summarized as follows:

1) The proposed microscopic model is effective in predicting the effective thermal conductivity of FRC, which is evidenced by the validations through comparisons with the FEM and the experimental results.
2) At the microscopic level, the temperature and heat flux at the interface of FRCs exhibit fluctuations during heat conduction, and the heat flux distribution inside the RVE is uneven, resulting in heat flux concentration.
3) The stochastic interface defects significantly reduce the effective thermal conductivity of fiber-reinforced composites, and the degree of reduction is proportional to the length and thickness of the defects.
4) The simulation results show that the area of the interface defect presents a strong linear correlation with the transverse thermal conductivity.
5) It is recognized that due to the complexity of the micro-structure of composite materials, thermal conductivity will inevitably be affected by other factors, such as fiber shape, internal porosity of the matrix, and the orientation and distribution of fibers, which were not considered in this study. Further research and more experiments will be carried out to improve our understanding of this complex issue.

Data availability statement

The raw/processed data required to reproduce these findings cannot be shared at this time as the data also forms part of an ongoing study.

CRediT authorship contribution statement

Yiwei Wang: Writing-original draft, Methodology, Visualization. Junjie Ye: Writing-review & editing, Methodology, Supervision. Lu Liu: Writing-original draft, Methodology, Visualization. Ziwei Li: Methodology, Validation. Yang Shi: Methodology, Conceptualisation. Juan M: Data curation, Visualization, Jianqiao Ye: Methodology, Conceptualisation, Supervision, Writing-review & editing.

Declaration of Competing Interest

The authors declare that they have no known competing financial interests or personal relationships that could have appeared to influence the work reported in this paper.

Acknowledgments

This work was supported by the National Natural Science Foundation of China, China (No. 52175112, 51675397). The 111 Project, China (No. B14042). Fundamental Research Funds for the

Central Universities (JB210421). China Scholarship Council (No. 202106960030).

References

[1] Wu JL, Song XP, Gong YZ, Yang W, He SJ, Lin J, Bian XM. Analysis of the heat conduction mechanism for al2o3/silicone rubber composite material with fem based on experiment observations. Compos Sci Technol 2021; 210(9):108809. DOI: 10.1016/j.compscitech.2021.108809.

[2] Adamczyk, Wojciech P., Sebastian Pawlak, Ziemowit Ostrowski. Determination of thermal conductivity of CFRP composite materials using unconventional laser flash technique. Measurement 2018; 124: 147-155. DOI: 10.1016/j.measurement.2018.04.022.

[3] Kosbe P, Patil P A. Effective thermal conductivity of polymer composites: A review of analytical methods. Int J Ambient Energy 2021; 42(8): 961-972. DOI: 10.1080/01430750.2018.1557544.

[4] Gori F, Corasaniti S. Effective thermal conductivity of composites. Int J Heat Mass Tran 2014; 77: 653-661. DOI: 10.1016/j.ijheatmasstransfer.2014.05.047.

[5] Li KQ, Li DQ, Liu Y. Meso-scale investigations on the effective thermal conductivity of multi-phase materials using the finite element method. Int J Heat Mass Tran 2020; 151: 119383. DOI: 10.1016/j.ijheatmasstransfer.2020.119383.

[6] David Müzel S, Bonhin E P, Guimarães N M, Guidi E S. Application of the finite element method in the analysis of composite materials: A review. Polymeers-Basel 2020; 12(4): 818. DOI: 10.3390/polym12040818

[7] Bakalakos S, Kalogeris I, Papadopoulos V. An extended finite element method formulation for modeling multi-phase boundary interactions in steady state heat conduction problems. Compos Struct 2021; 258: 113202. DOI: 10.1016/j.compstruct.2020.113202.

[8] Gu Y, Hua QS, Zhang CZ, He XQ. The generalized finite difference method for long-time transient heat conduction in 3D anisotropic composite materials. Appl Math Model 2019; 71: 316-330. DOI: 10.1016/j.apm.2019.02.023.

[9] Ye JJ, Wang YW, Li ZW, Saafi M, Jia F, Huang B, Ye JQ. Failure analysis of fiber-reinforced co mposites subjected to coupled thermo-mechanical loading. Compos Struct 2020; 235:111756. DOI: 1 0.1016/j.compstruct. 2019.111756.

[10] Taheri-Behrooz F, Pourahmadi E. A 3D RVE model with periodic boundary conditions to estimate mechanical properties of composites. Struct Eng Mech 2019; 72(8):713-722. DOI: 10.12989/sem. 2019.72.6.713.

[11] Babu K P, Mohite P M, Upadhyay C S. Development of an RVE and its stiffness predictions based on mathematical homogenization theory for short fiber composites. Int. J. Solids Struct 2018; 130:80-104. DOI: 10.1016/j. ijsolstr. 2017.10.011.

[12] Tian WL, Qi LH, Chao XJ, Liang JH, Fu M. Numerical evaluation on the effective thermal conductivity of the composites with discontinuous inclusions: Periodic boundary condition and its numerical algorithm. Int J Heat Mass Tran 2019; 134:735-751. DOI: 10.1016/j.ijheatmasstransfer.2019.01.072.

[13] Wang H, Qin QH. A new special coating/fiber element for analyzing effect of interface on thermal conductivity of composites. Appl Math Comput 2015; 68(6):311-321. DOI: 10.1016/j.amc.2015.06.077.

[14] Zhao XY, Tu WQ, Chen Q, Wang GN. Progressive modeling of transverse thermal conductivity of unidirectional natural fiber composites. Int J Therm Sci 2021; 162:106782. DOI: 10.1016/j.ijthermalsc i.2020.106782.

[15] Vieira C, and Marques S. A new three-dimensional finite-volume model for evaluation of thermal conductivity of periodic multiphase composites. Int J Heat Mass Tran 2019; 139:412-424. DOI: 10.1016/j.ijheatmasstransfer.2019.05.031.

[16] Shiah YC, Shi YX. Anisotropic heat conduction across an interface crack/defect filled with a thin interstitial medium. Eng Anal Bound Elem 2006; 30:325–337. DOI: 10.1016/j.enganabound.2006.01.012.

[17] Ochiai Y. Three-dimensional heat conduction analysis of inhomogeneous materials by triple-reciprocity boundary element method. Theor Apply Fract Mec 2015; 51:101-108. DOI: org/10.1016/j.enganabound.2014.10.014.

[18] Fahmy M A. A new boundary element formulation for modeling and simulation of three−temperature distributions in carbon nanotube fiber reinforced composites with inclusions. Math Method Appl Sci 2021; 1-16. DOI: 10.1002/mma.7312.

[19] Oberg M, Anflor C T M, Goulart J N V. Using BEM to predict the effective thermal conductivity for heterogeneous materials. Revista de Engenharia Térmica 2015; 14(1):09-15. DOI: 10.5380/reterm.v14i1.62107.

[20] Wang HT, Yao ZH. Large-scale thermal analysis of fiber composites using a line-inclusion model by the fast boundary element method. Eng Anal Bound Elem 2013; 37(2):319–326. DOI: 10.1016/j.enganabound.2012.11.007.

[21] Dong CY. An interface integral formulation of heat energy calculation of steady state heat conduction in heterogeneous media. Int J Heat Mass Tran 2015; 90:314-322. DOI: 10.1016/j.ijheatmasstransfer.2015.06.066.

[22] Qu XY, Dong CY, Bai Y, Gong YP. Isogeometric boundary element method for calculating effective property of steady state thermal conduction in 2D heterogeneities with a homogeneous interphase. J Comput Appl Math 2018; 343(1):124-138. DOI: 10.1016/j.cam.2018.04.053.

[23] Gong YP, Dong CY, Qu XY. An adaptive Isogeometric boundary element method for predicting the effective thermal conductivity of steady state heterogeneity. Adv Eng Softw 2018; 119(5):103-115. DOI: 10.1016/j.advengsoft.2018.03.001.

[24] Sapucaia V W, Pereira A M B, Leiderman R. Pixel-based boundary element method for computing effective thermal conductivity of heterogeneous materials. Eng Anal Bound. Elem 2023; 149:298-308. DOI: 10.1016/j.enganabound.2023.01.014.

[25] Drake DA, Sullivan RW. Prediction of delamination propagation in polymer composites. Compos Part A Appl Sci 2019; 124:105467. DOI: 10.1016/j.compositesa.2019.05.035

[26] Cai H, Ye JJ, Wang YW, Shi Y, Saafi M, Ye JQ. Microscopic failure characteristics and critical length of short glass fiber reinforced composite. Compos Part B-Eng. 2023; 266:110973. DOI: 10.1016/j.compositesb.2023.110973.

[27] Hasselman D P, Johnson L F. Effective thermal conductivity of composites with interfacial thermal barrier resistance 1987; 21:508-515. DOI: 10.1177/002199838702100602.

[28] Islam M, Pramila A. Thermal conductivity of fiber reinforced composites by the FEM. J Compos Mater 1999; 33(18):1699-1715. DOI: 10.1177/002199839903301803.

[29] Youngblood G E, Senor D J, Jones R H, Graham S. The transverse thermal conductivity of 2D-SiCf/SiC composites. Compos Sci Technol 2002; 62(9):1127-1139. DOI: 10.1016/S0266-3538(02)00069-6.

[30] Whitehouse AF, Clyne TW. Effects of reinforcement contact and shape on cavitation and failure in metal-matrix composites. Compos 1993; 24:256-61. DOI:10.1016/0010-4361(93)90172-5

[31] Sokołwski D, Kamiński M. Computational homogenization of carbon/polymer composites with stochastic interface defects. Compos Struct 2018; 183:434-49. DOI: 10.1016/j.compstruct.2017.04.076

[32] Ding J, Ma X, Fan X, Xue J, Ye F, Cheng L. Failure behavior of interfacial domain in SiC-matrix based composites. J Mater Sci Technol 2021; 88:1-10. DOI: 10.1016/j.jmst.2021.02.010

[33] Kolpakov AA, Kolpakov AG. Capacity and Transport in Contrast Composite Structures: Asymptotic Analysis and Applications. Boca Raton: CRC Press; 2010.

[34] A. J. Goupee, S. S. Vel, Multiscale thermoelastic analysis of random heterogeneous materials: Part II: Direct micromechanical failure analysis and multiscale simulations, Computational Materials Science 48 (2010) 39–

53. DOI: 10.1016/j.commatsci.2009.10.004.

[35] Brebbia C A, Telles J C F, Wrobel L C. Boundary Element Techniques, Springer-Verlag, Berlin, 1984.

[36] Chen Q, Zhai Z, Zhu XJ, Xu CB, Chen XF. Numerical simulation of strain rate effect on the inelastic behavior of metal matrix composites. Sci Eng Compos Mater 2017; 24(2):279-288. DOI: 10.1515/secm-2015-0133.

[37] Yang TY, Chen WJ, Hu JH, Zhao HB, Fang GQ, Peng FJ, Cao ZL. Thermal conduction behaviors of single-ply broken twill weave reinforced thermally induced resin-based shape memory polymer composites: Multi-scale method analysis and laser flash analysis. Appl Compos Mater 2022; 49:473–496. DOI: 10.1007/s10443-021-09977-w.

[38] Springer S G, Stephen W T. Thermal conductivities of unidirectional materials. J Compos Mater 1967; 1(6):166-173. DOI: 10.1177/002199836700100206.

[39] Berlyand L, Kolpakov AG, Novikov A. Introduction to the Network Approximation Method for Materials Modeling. Cambridge: Cambridge University Press; 2013.

[40] Zahid M, Sharma R, Bhagat A R, Abbas Syed, Kumar A, Mahajan P. Micro-structurally informed finite element analysis of carbon/carbon composites for effective thermal conductivity. Compos Struct 2019; 226: 111221. DOI: 10.1016/j.compstruct.2019.111221.

[41] Wang P, Wang KF, Wang BL, Cui YJ. Effective thermoelectric conversion properties of thermoelectric composites containing a crack/hole. Compos Struct 2018; 191:180-9. DOI: 10.1016/j.compstruct.2018.02.049

[42] Kamiński M. Stochastic problem of fiber-reinforced composite with interface defects. ENG COMPUTATION 2002; 19(7): 854-868. DOI:10.1108/02644400210444348

[43] Freedman D, Diaconis P. On the histogram as a density estimator: L2 theory. Zeit Wahr ver Geb 1981; 57:453–476. DOI: 10.1007/bf01025868.